MINISTRY OF EDUCATION
National University of Science and Technology
POLITEHNICA Bucharest
DOCTORAL SCHOOL OF MECHANICAL AND MECHATRONIC ENGINEERING

PHD THESIS SUMMARY

RESEARCH ON LASER PLASMA PROTON ACCELERATORS FOR RADIOTHERAPY OF MALIGNANT TUMORS

PhD supervisor:
Prof. Dr. Eng. Octavian DONȚU

Author:
MSc. Eng. Alexandru LAZĂR

BUCHAREST
2023

CONTENT

List of notations

RF-LINAC	radio frequency linear accelerator
PBT	proton beam therapy
LET	linear energy transport
CERN	European Center for Nuclear Research
LPA	laser plasma accelerator
CPA	chirped pulse amplification
Ti:Sapphire	sapphire doped with titanium ions
SAC	American Cancer Society
OPCPA	optical parametric amplification chirped pulses
BELLA	Berkeley Laboratory Laser Accelerator
PIC	particles in cells
ELI	Extreme Light Infrastructure
TNSA	target normal sheath acceleration
Nd:YAG	yttrium aluminum garnet doped with neodymium ions
FTL	Fourier transform limit
FWHM	full width at half maximum
OPA	parametric optical amplification
ASE	amplification of spontaneous emission
CR-39	detector with polycarbonate radiation-sensitive material
RCF	detector for radiochromic film imaging spectroscopy
TP	Thomson Parabola spectrometer
PMQ	quadrupoles permanent magnet
EMQ	quadrupoles electromagnet
TEM_{00}	transverse electromagnetic
GVD	group velocity dispersion
GDD	group delay dispersion
SF11	dispersive optical medium
AO	acousto-optic device
BBO	barium beta borate
SHG	second harmonic generation
EO	electro-optical device
MO	magneto-optical device
STL	standard triangle language
PLA	polylactic acid
GUI	graphical user interface
KTP	potassium titanyl phosphate
$(C_8H_8)_n$	polystyrene
HSV	huge saturation value

INTRODUCTION

1. Scientific motivation

The laser plasma proton accelerator will be composed of a high-power laser system [23,24], a proton beam acceleration system [25-28] and a proton beam control and orientation system in the room treatment [29-32]. The constructive solution of the proton accelerator in laser plasma for the radiotherapy of malignant tumors, aims to automate some processes that have the role of reducing the temporal and spatial instabilities of the proton beams. The proton accelerator was designed based on the results of the analytical calculation elements carried out following specialized research on the operation mode of high-power laser systems. Closed-loop control systems were designed based on the results of experimental research on position guidance and automatic energy control of laser beams. The proton beam generation process was investigated by interpreting the simulation results regarding the interaction of the laser beam and the solid target that served as the proton source. The proton beam control and transport system in the treatment room was investigated based on the results of simulations on the dynamic behavior of the proton beam depending on the energy and the direction of propagation.

2. The need of research within the thesis

Currently, several types of ionizing radiation [34] are used to treat malignant tumors. Of these, high-energy proton beams are among the most effective beams for radiotherapy. Unique properties of proton beams determine the advantages of this type of radiotherapy over irradiation with photons, electrons and other types of radiation shown in fig. 1. To deliver a therapeutic dose at an adequate penetration distance, accelerators and beam control systems must be able to generate proton energies in the 100 MeV - 250 MeV range.

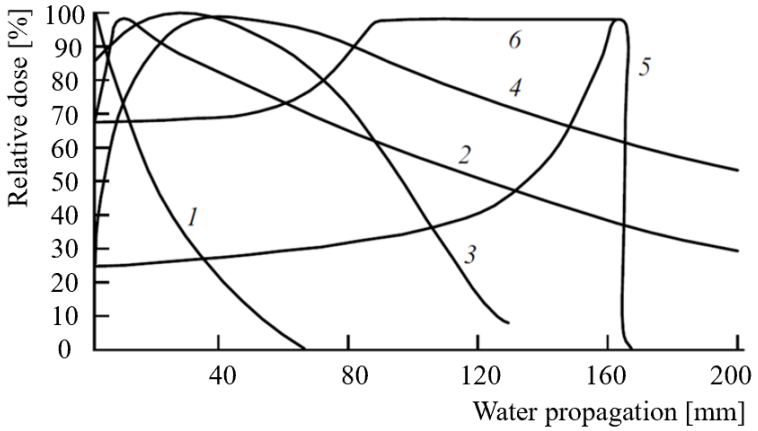

Fig. 1. Dose distribution during water propagation of different types of radiation: 1-X-rays, 140 keV; 2-gamma radiation from cobalt isotopes (60Co), 17 keV; 3-electron beam, 25 MeV; 4-bremsstrahlung radiation, 25 MeV; 5-monochromatic proton beam, 160 MeV (Bragg curve); 6-modified Bragg curve, the energy spectrum of the beam is controlled and tuned for uniform irradiation of the biological target at a penetration distance of 90 to 160 mm, figure adapted from [34].

The advantages of using proton beams for the radiotherapy of malignant tumors come from the following specific characteristics such as:

- ✓ Propagation in the patient's biological tissue is energy dependent and makes it possible to stop the beam at a predetermined penetration distance [41, 42].
- ✓ Protons have a smaller divergence than gamma rays, so they are easier to collimate.
- ✓ Ionization losses increase with penetration distance and reach a maximum at the point where the particle stops, giving rise to the so-called Bragg peak [43].
- ✓ Minimizing damage to healthy tissues around the tumor.

These characteristics of the interaction of the proton beam with biological tissues determine the advantages of this type of radiotherapy.

Currently, high power laser systems open new opportunities to be used as particle accelerators [1] with revolutionary impact in several fields [38]. Compared to RF-Linac [41] which uses electromagnetic fields generated by high voltage sources, laser plasma particle accelerators use electromagnetic fields generated by laser beams to accelerate particles [46].

Advantages of using laser plasma particle accelerators are:

- ✓ Complexity and gauge dimensions are reduced.
- ✓ Particles are accelerated distances of a few micrometers.
- ✓ Implementation and operating costs are reduced.
- ✓ Produces proton beams with broad spectral energy band.

3. Structure and objectives of the thesis

The objectives imposed in the design stage of the laser system that will be used to accelerate proton beams are: 1) obtaining laser beam intensities of 10^{20}-10^{21}W/cm^2, 2) automating some processes within the high-power laser system for stability control, spatial and temporal patterns of the laser beam and implicitly the proton beam, and 3) designing the high power laser system at a repetition rate of at least 5 Hz.

The main objectives pursued within the proton beam generation system that will be able to be used for radiotherapy of malignant tumors are: 1) research of the interaction between the laser beam and the target, 2) simulation of the proton beam generation process, 3) obtaining a number of protons greater than 10^6 per pulse in the generated energy spectrum.

The research on the control system of the spatial distribution profile and orientation of the direction of propagation in the proton beam treatment room aims to achieve the following objectives: 1) simulation of the dynamic behavior of the proton beam during its propagation through the system and 2) the possibility of energy modulation through the control and transport system.

To achieve the proposed objectives, research was carried out in specialized literature in several fields such as: the physics of high-power lasers, the engineering of particle accelerators and medical science, respectively the oncology field. So, the thesis was structured in seven chapters as follows.

CHAPT. 1. SOME PROBLEMS REGARDING THE ACCELERATION OF PROTON BEAMS FOR RADIOTHERAPY OF MALIGNANT TUMORS

Despite the advantage that the radiation dose of the proton beam [43] is the most compliant for tumor therapy, compared to other accelerated particle beams [39, 40], currently only a few dozen centers around the world provide beams of ions. Their large-scale implementation is hindered by their large size and high cost. For this reason, efforts are being made to develop compact and reliable systems for proton radiotherapy.

1.1. Radio frequency accelerators currently in use

1.1.1. Manufacturing, technological difficulties and high costs

A compact advanced carbon ion RF-Linac that accelerates beams to energy that is sufficient for radiotherapy is approximately 45 m [58] and is proposed to deliver a full energy of 450 MeV/u, which exceeds the maximum energy required for carbon ions radiotherapy. It is also capable of accelerating protons and many other ion species to the same energy per nucleon [59]. Even though the development of superconducting cyclotrons [60] for proton radiotherapy has led to a reduction in size and weight, the manufacturing costs of essential components still remain high. Currently, the smallest proton beam therapy system is approximately 2600 m^3 in volume with a 190 m^2 footprint and can accelerate protons up to 230 MeV.

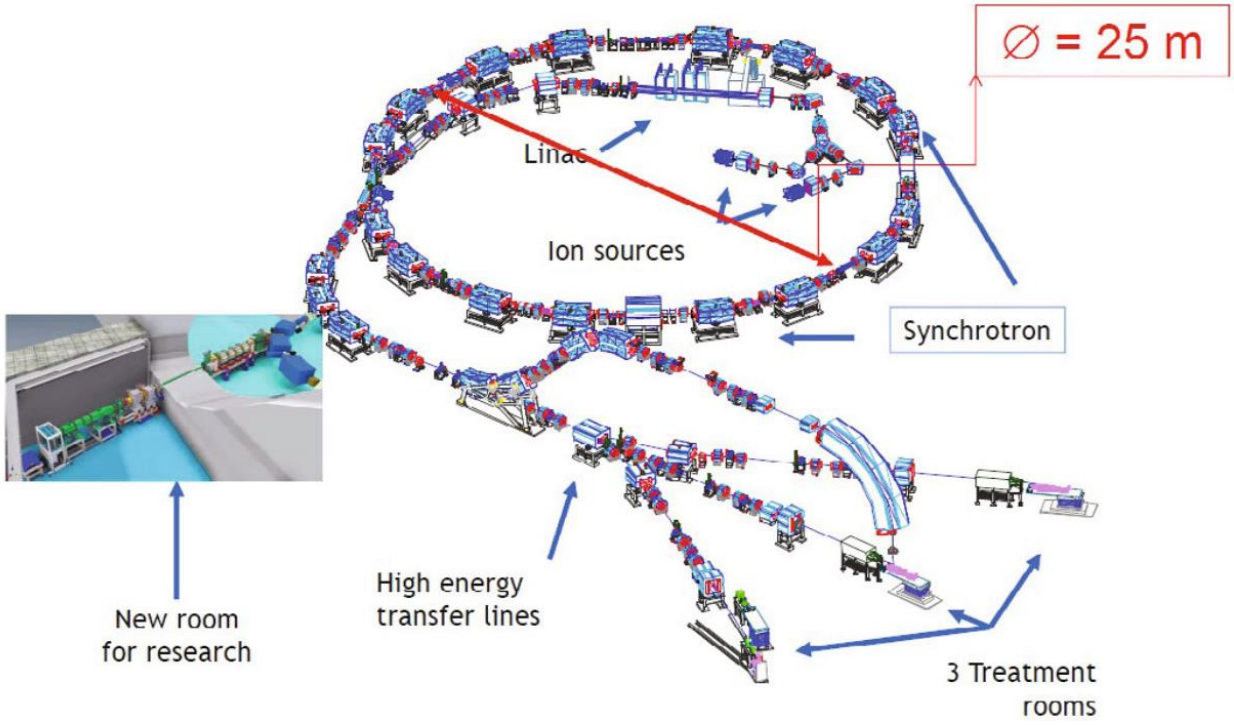

Fig. 1.1. Model of an ion (proton) accelerator in RF for radiotherapy of malignant tumors [62].

A medical center for hadronic therapy was built in Pavia (Italy), which was the second institution in the world to offer carbon ion radiotherapy treatment after the one in Japan [67]. The Pavia system was developed based on a study of proton-ion radiotherapy carried out at the European Center for Nuclear Research (CERN) [68]. CERN has proposed a facility consisting of a static synchrocyclotron, where proton beams are energy-selected [69], for quadrupole magnet-based hadron therapy at 750 MHz radio frequency. In collaboration with CERN, the Center for Research and Development in Hadron Therapy is building prototypes of the new structures [70] where the electric field intensity reaches 50 MV/m, to control and direct the particle beams in linear accelerators with high precision. The same applies for carbon ion oncology therapy, which has also been studied in collaboration with CERN [71].

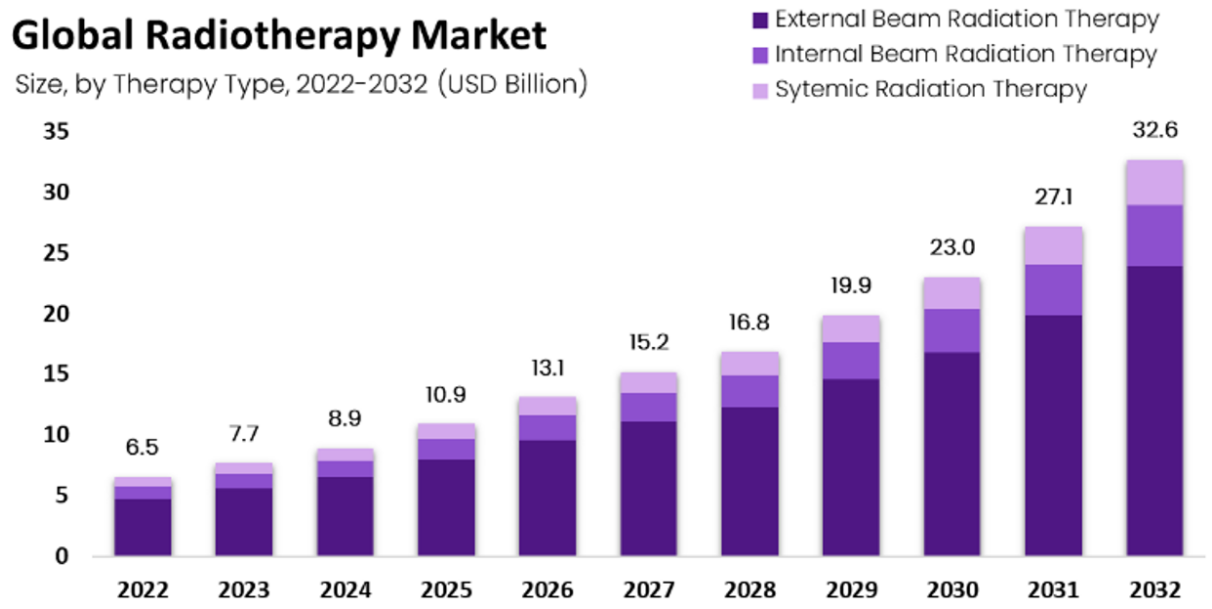

Fig. 1.2. Industry Segment Outlook, Market Assessment, Competition Scenario, Trends, and Forecast 2023-2032, Regarding Global Radiotherapy Market, figure adapted from [73].

The global radiotherapy market size is estimated to be worth approximately $32.6 trillion during 2023-2032, scaling up from $6.5 trillion in 2022 [72]. Global radiotherapy market is classified (Fig. 1.2.) by type of therapy (external beam radiotherapy [74], internal beam radiotherapy [75] and systemic radiotherapy), by application (malignant prostate tumor, malignant breast tumor, malignant tumor of lung, malignant brain tumor, malignant neck tumor, malignant colon tumor, malignant cervical tumor, and others [76]), by end users, by region and by companies.

1.1.2. Limited acceleration field strength

Due to vacuum decay limitations, the acceleration field is limited. Acceleration fields can induce interactions between accelerated particles and gas molecules in the system through which they propagate. These interactions can lead to the production of secondary particles and radiation, which can affect beam quality or damage accelerator components.

Acceleration fields can generate significant amounts of energy and heat. If the field strength is too high, overheating and damage to accelerator components may occur [58]. This can lead to high maintenance and repair costs.

1.1.3. Long particle acceleration distances

Particle accelerators are large [74], often of tens of meters or even of hundreds of meters, for several reasons. To accelerate particles to very high energies, a long distance is required to give them enough time to gain the desired energy when propagating through the electric or magnetic fields generated by the accelerator components.

1.1.4. Statistics on medical centers for proton and ion beam radiotherapy

The medical field has nowadays become dependent on particle accelerators because they are the most effective tools used to treat malignant tumors [92, 93]. Each year, the American Cancer Society (ACS) estimates the new cases of malignant tumors and deaths, based on the population. For example, in the United States in 2023, it is estimated that there will be 1,958,310 new cases of malignant tumors and 609,820 deaths from malignant tumors [94].

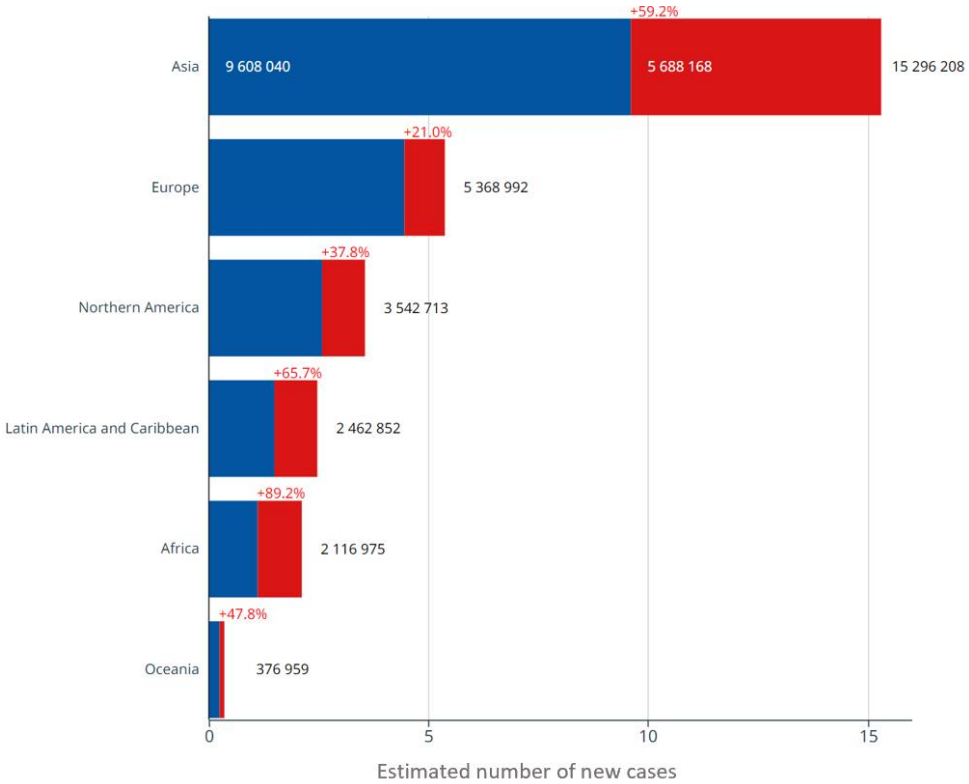

Fig. 1.3. Estimated number of new cases of malignant tumors from 2020 to 2044, for all types of malignant tumors, both sexes, all ages. Figure adapted from [94].

Malignant tumor is a complex pathology that manifests itself through the uncontrolled division of tumor cells, but it can also lead to affecting the function of the tissues in which it

develops or metastasizes. The number of patients (Fig.1.3.) who should be treated using radiotherapy is far too high compared to those who have access to it. Ongoing research and development to help overcome this impediment, including improving treatment efficiency and effectiveness, is advancing. An estimated number of 191 radiotherapy medical centers will be available by the end of 2026 [64]. Currently, only 121 of these are available for radiotherapy, 38 are under development and 35 are in the design phase (Fig. 1.4.).

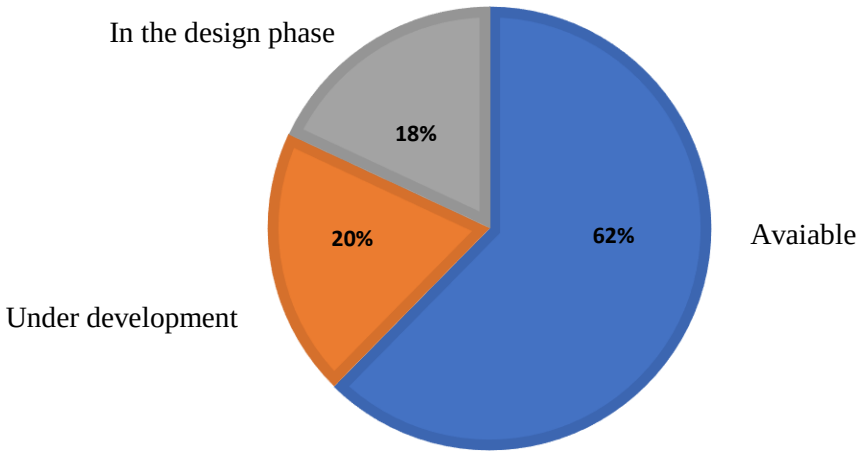

Fig. 1.4. Statistics of medical centers available (blue), under development (orange) and in the design phase (grey) for proton and ion radiotherapy.

1.2. Laser plasma proton accelerators

Currently, active work is being done to design the so-called laser plasma proton accelerators [91]. A high-power laser pulse incident on a solid target can produce proton beams of various energies [1]. The main challenge faced by plasma-laser accelerator design experts is obtaining particle energies in the 200-250 MeV range instead of the currently available 100 MeV [18, 19].

1.2.1. Peak power limitation of laser systems

In March 2019, the high-power laser system installed within the ELI project in Romania generated the first pulses at a power level of 10 PW being a world record [106]. In August 2020, for the first time in the world, ten consecutive pulses of 10 PW (240 J/23 fs) [109] reached the research chambers of the facility after propagation through the beam control and transport system. One of these chambers will be dedicated to accelerating electrons, with the aim of reaching energy levels of tens to hundreds of GeV [107]. The other experimental chambers will be used for accelerating protons and ions and for research aimed to understanding the fundamental mechanisms of nuclear physics, such as the formation of matter in the heart of stars, the very origin of life as we know it [108].

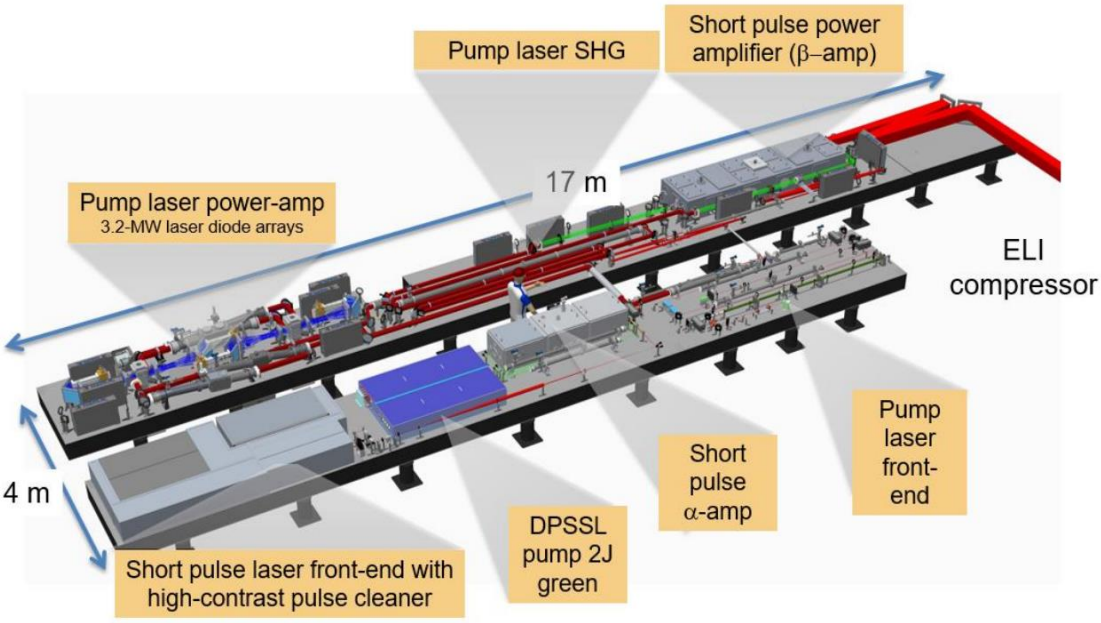

Fig. 1.5. Schematic of the Czech PW class laser system [110].

The ELI facility in the Czech Republic is to complete the fourth high-power laser (Fig. 1.5), which will accelerate particles in laser plasma to energies greater than 10 GeV with an ultrashort time duration [110].

1.2.4. Reproducibility and repetition rate

Current high-power laser systems operate at repetition rates of a few Hz, and the technologies for laser-plasma acceleration, laser beam control, its diagnostics, [128] will have to be adapted to high repetition rates (tens of kHz). Laser plasma acceleration of particle beams [127] at a repetition rate of 1 Hz showed significant variations in energy from one pulse to another [129].

At the present time, research on the techniques and mechanisms of laser plasma acceleration [18, 19] of protons are under development [130]. So far, no experimental results with reproducible beam have been reported. Most researchers study and propose different solutions [131] in order to have the best possible result regarding the required energy of the proton beams and their reproducibility [1].

1.3. Conclusions on radiofrequency accelerators and the possibility of using laser plasma accelerators for proton beam radiotherapy

Even though laser plasma accelerators provide pulsed beams with a low repetition rate, the accelerated beam has a high number of protons per pulse and the energy spectra is large. In the future, closed-loop control systems will allow high stability, control, and precision at higher repetition rates in the order of kHz [128], by using learning and artificial intelligence methods [146-148]. The development of a LPA at repetition rates in the order of kHz will be a key step towards the application of this acceleration technology in several fields.

CHAPT. 2. THE CURRENT STATE REGARDING THE ACCELERATION OF PARTICLES WITH HIGH POWER LASER BEAMS

Laser plasma accelerators [127, 126] are capable of producing acceleration fields of 10–100 GeV/m, which is 100–1000 times higher than those generated using conventional technology. LPA accelerates particles over distances of several orders of magnitude shorter than thr radio frequency technology. This leads to the reduction of braking radiation "bremsstrahlung" [37, 40] and therefore to the reduction of the total energy consumption to reach the desired energy. These properties of LPA open a new horizon for compact and less expensive high-energy particle accelerators.

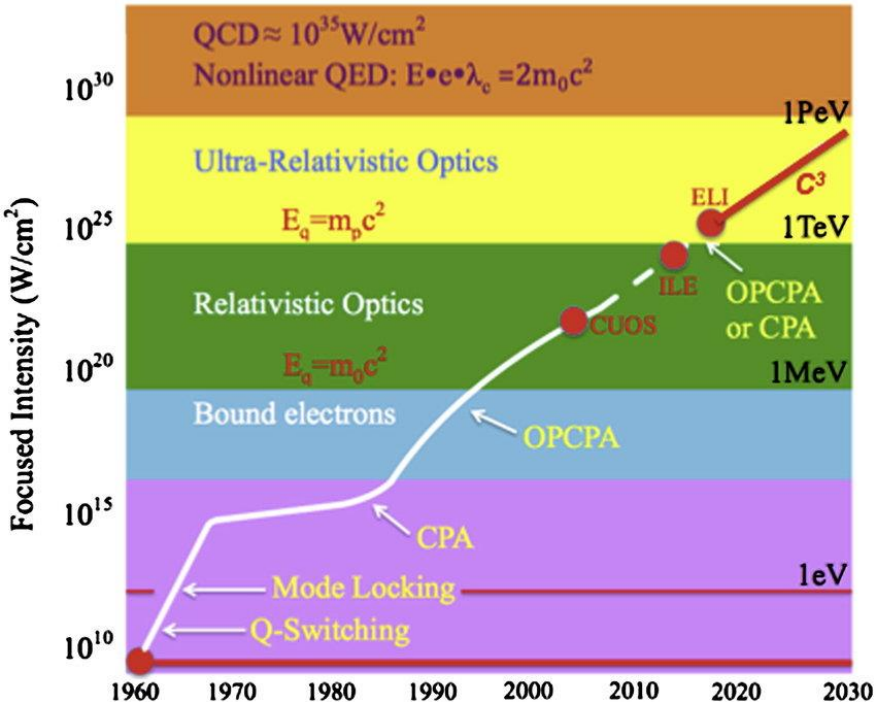

Fig. 2.1. Time evolution of beam intensity, figure adapted from [195].

Within the European Laser Laboratory, a research and development plan for LPA has been developed that extends to the year 2045. The target of this research is to provide a perspective of LPA with significantly reduced dimensions, which could be an alternative way to accelerate particles on the TeV-MeV scale [27, 28]. These accelerators offer the prospect of compact and cost-effective short-term particle physics experiments with new physical possibilities that contribute to precision research and the search for new particles.

The key elements of a LPA [126] are the development of techniques for generating plasma effects [38] and reducing the plasma density to control and tune the phase velocity of the plasma wave [57]. Minimizing the chromatic emission associated with beam divergence or emittance is a critical issue [94]. Methods of mathematical description of the plasma-based laser beam should be addressed to solve this problem. Particle acceleration to GeV energies [18] is the highest short-term research priority for LPA development [95].

2.1. Research on the operation mode of high-power laser systems

High-power lasers based on the CPA operation method [156], can generate laser pulses at the PW level [27] which make possible the experimental research of nonlinear processes in atomic, molecular, plasma, solid state physics and the research of unexplored states of matter. The CPA method of operation [149] requires the ultrashort laser pulse to be temporally increased, amplified in energy, and then shortened to the pulse duration given by the oscillator (Fig. 2.2).

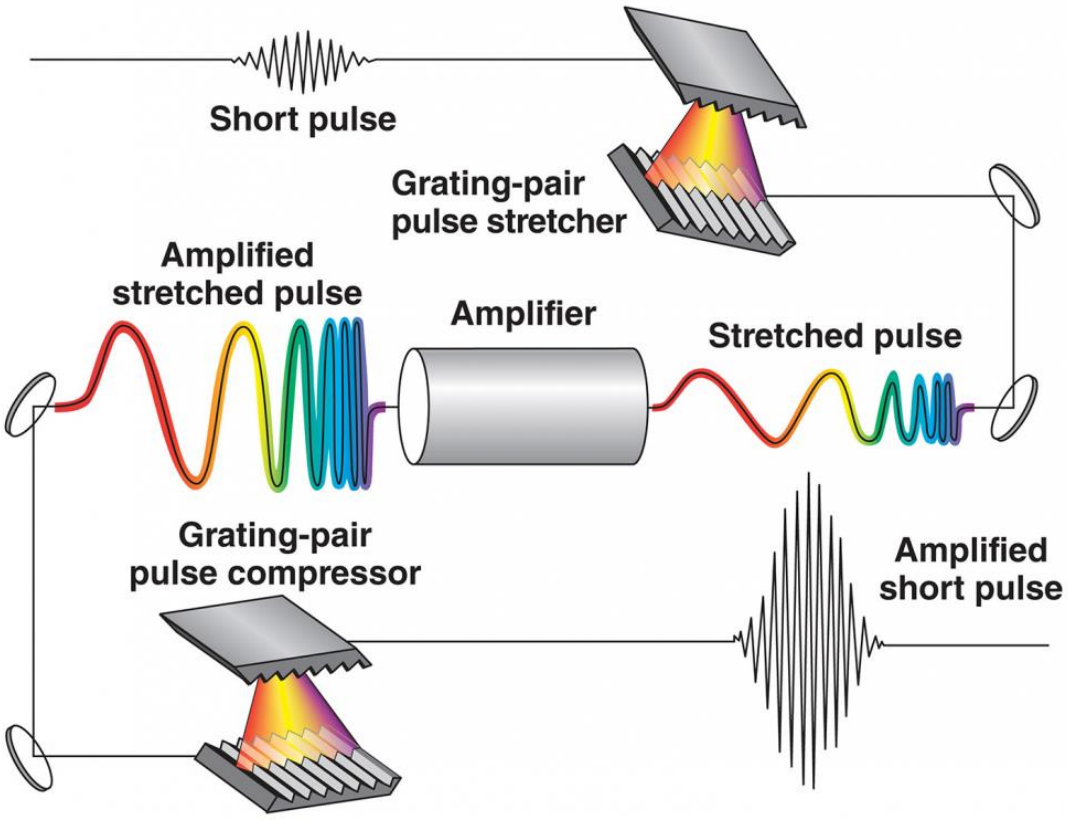

Fig. 2.2. Obtaining high-power laser pulses by the CPA method, [University of Rochester – Energy Laser Laboratory] [84].

Ultrashort (femtosecond) laser pulses [135, 136] are obtained in a laser oscillator by the all-wavelength phase-coupling method. The optical system for increasing the pulse duration [132, 133, 134] uses diffraction gratings to control and adjust the temporal profile of the laser pulse. This stage of the CPA method [149], makes it possible to amplify the laser pulses [118, 119] to energies of hundreds of J. Finally, the optical temporal shortening system [95, 16] will return the duration of the laser pulse to a value close to that of the ultrashort pulse oscillator.

For these laser systems, the main challenges are the fabrication of large-sized optical components [158] (diffraction gratings for temporal shortening [96], mirrors for laser beam orientation, deformable mirrors for wavefront correction, amplification, its focus) and laser beam characterization.

2.1.1. The phenomena underlying the generation of ultrashort laser pulses

The time interval of ultrashort laser pulses is 10^{-14} - 10^{-16} seconds, during which some processes in physics, chemistry and biology take place (Fig. 2.3) [159]. Obtaining such time durations for laser pulses became possible with the development of polychromatic laser beam generation technique. Most oscillators with ultrashort laser pulses can provide pulses with order durations of tens-hundreds of fs [160]. To understand how short the laser pulse is, we can say that the event of a process lasting one fs, compared to one second, is equivalent to 8 minutes of the age of the universe. The distance that the visible light can travel in a fs is several hundred nanometers, equivalent to the atomic distance of several thousand elementary particles in a solid. This suggests the importance of the fs time scale relative to the microcosmos.

The unique properties of ultrashort light pulses [126] open new possibilities of understanding matter because energy can be concentrated in an ultrashort time interval, which allows the study of a dynamical system with extraordinary temporal resolution. Even at low energies, the pulse power can be very high.

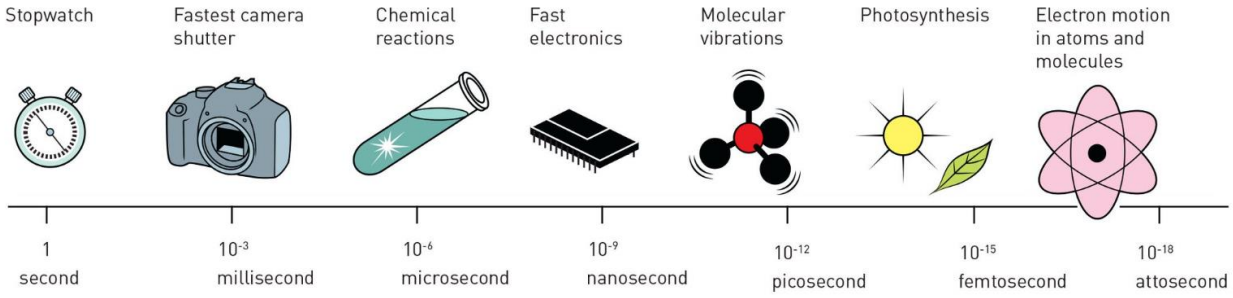

Fig. 2.3. Highlighting the reaction time of various mechanical, electronic, chemical, biological and physical events. Figure adapted from reference [149].

For example, if the laser pulse has a duration of 1 fs, at an energy of 1 mJ, i.e. $\approx 3 \cdot 10^{15}$ photons with a wavelength of λ= 800 nm, has an average power of 1 terawatt. Focusing a pulse like this into a diameter of 10 μm^2 produces an intensity of $1 \cdot 10^{15}$ W/cm^2, i.e. approximately 3 GV/cm, intensity for the electric field. Another important characteristic for ultrashort pulses is the spatial length related to the coherence phenomenon. Due to the stable temporal phases that are present in the electromagnetic field (Fig. 2.4) the coherence condition is fulfilled.

2.2. Research on the acceleration of proton beams in laser plasma

Proton beams are formed (red) on a thin material substrate (green) when a short and intense laser pulse (yellow) is incident on the target surface (Fig. 2.4. a). Electrons moving through the target (blue) are accelerated to relativistic energies (a) and generate an electrostatic field that accelerates protons (Fig. 2.4. b), due to the non-uniformity of the electron field in the transverse and radial planes (Fig. 2.4. c) .

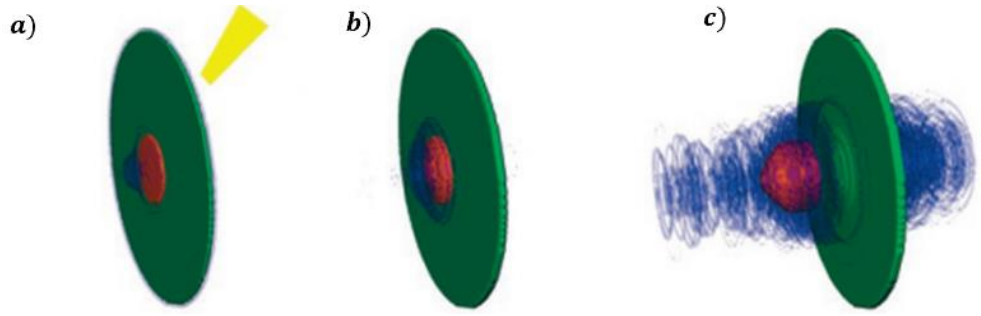

Fig 2.4. Illustration of the steps of proton acceleration on the surface of a thin target irradiated with a laser beam. a) laser-target interaction, b) electrostatic field generation, c) proton acceleration [255].

2.2.1. The phenomena involved in the process of particle acceleration

The main forces induced by the laser beam in the plasma, which are capable of accelerating ions to very high velocities over short distances can be briefly divided into electromagnetic forces [193] and hydrodynamic or thermal pressure forces [194]. The electromagnetic forces involved are laser pulses with high intensities 10^{15} W/cm^2 and respectively laser pulses with very high 10^{18} W/cm^2 (these are relativistic intensities- when an electron placed in this medium acquires velocities comparable to the speed of light) that interact with the plasma. The field induced by the electromagnetic forces generated by the laser can reach extreme values of the electric field intensity (> 100 GV/cm). As a result, these forces can accelerate ions to high speed over distances shorter than a mm. The electromagnetic forces that can accelerate ions in laser plasma to high and very high intensities can be simply described by the Lorentz equation [195]:

$$F = qE + q(v \times B) \tag{2.1}$$

Where: q is the particle charge, v is the particle velocity, and E and B are the electric and magnetic components of the electromagnetic field in the plasma. This force interacting with electron plasma and ion plasma is called the ponderomotive force. The electrons are pushed away from the ions (from the equilibrium position) by the gravitational force, leading to the creation of a huge electric field between the moving electron particles and the ions. This electric field accelerates the ions, which usually move along with the electron particles.

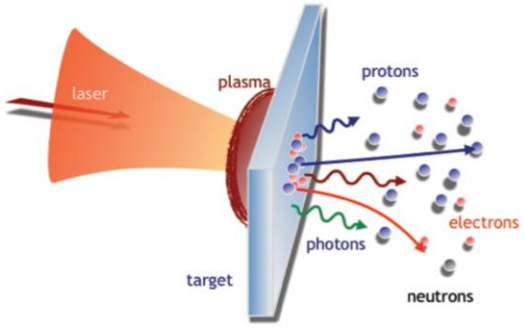

Fig. 2.5. Simplified scheme of the laser-hold interaction mechanism for ion acceleration [141].

2.2.3. Techniques for characterizing temporal and spatial properties

The experimental scheme in which the CR-39 detectors were used was carried out in the attosecond laser beam research laboratory in Szeged, Hungary [220]. The 12 fs, 35 mJ, linearly polarized laser beam was focused onto a 2 μm aluminum target from which an accelerated proton beam was obtained (Fig. 2.6). Spatial characterization of the proton beam was performed by proton beam projection imaging through a periodic grating [221], consisting of a copper mesh, having a thickness of 20 μm.

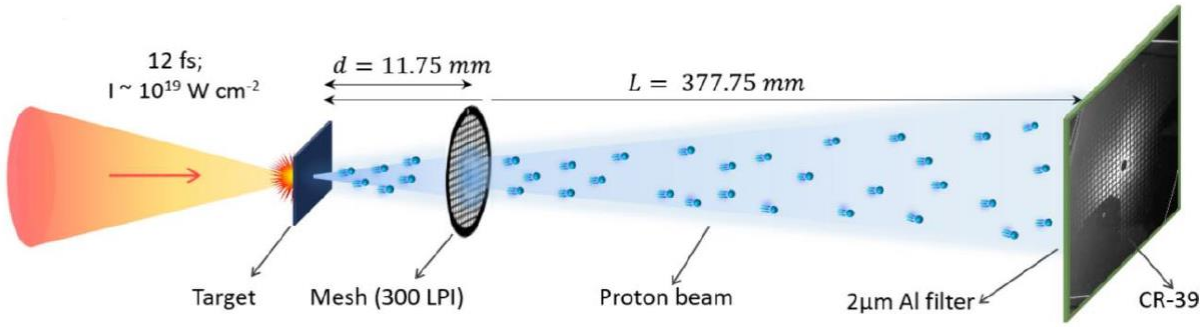

Fig. 2.6. Scheme of the proton beam generating system using a high power laser beam. The image of the periodic lattice is projected onto the CR-39 detector using the accelerated proton beam [219].

The laser beam area measured at FWHM was 2.9 μm × 3.5 μm, from which an estimated maximum intensity of 10^{19} W/cm^2 was obtained (Fig. 2.7 a). Fig. 2.26 b shows the raw image of the particle tracks, where protons dominate over other ion species such as carbon or oxygen. The corresponding estimated kinetic energy spectrum (Fig. 2.7 c) of the proton beam shows an energy reduction of 0.5 MeV. To avoid saturation of the CR-39 plate with low energy protons and carbon ions, a 2 μm thick aluminum filter was used in front of the CR-39 detector. This filter can block protons up to 225 keV (shown by the vertical line in Fig. 2.7 c) and carbon ions up to 1.8 MeV [222].

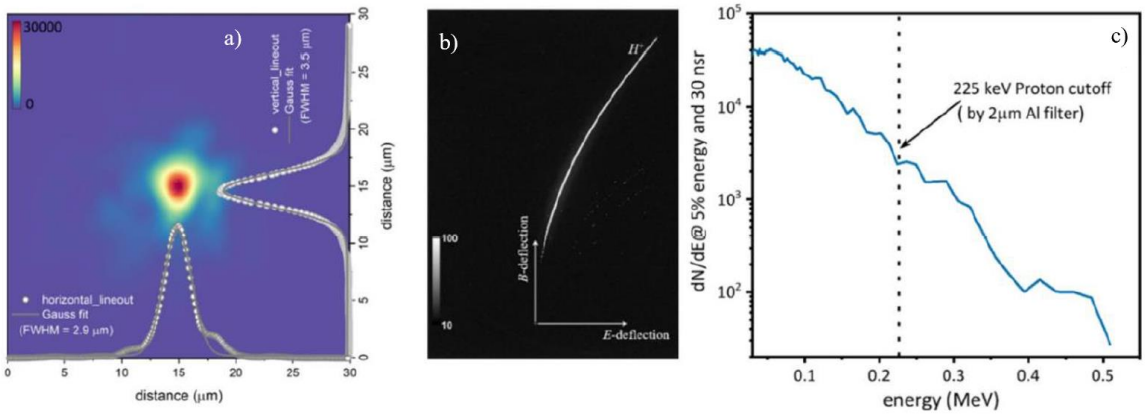

Fig. 2.7. Focused laser beam intensity distribution (b). Magnetic and electric field deflection of the proton beam (b) and calculated kinetic energy spectrum (c) [219].

2.4. Outlook on the use of laser plasma proton accelerators for medical Applications (2024)

Currently, there is no functional medical center for radiotherapy of malignant tumors with accelerated proton beams in laser plasma [126], as this new technology is under research. The development of centers for radiotherapy of malignant tumors with accelerated proton beams in laser plasma is of great interest due to the advantages that these types of radiation have [43]. Research efforts are currently underway to understand and apply these technologies in the near future. Many research institutions in Europe, Asia and America study the acceleration of protons in laser plasma through different mechanisms and propose several solutions for the characterization of accelerated particles. Performance validation and optimization of these possible systems for radiotherapy treatments are in the testing phase.

Fig. 2.8 shows the laser plasma accelerator that can generate and control proton beams of energies lower than 10 MeV [223]. High electrical current proton beams with a continuous energy spectrum and large divergence angle is generated through a high contrast laser beam and micron-thick targets. The emitted beam is subsequently collected, analyzed, and focused by a control and transport system using quadrupole electromagnets and dipole magnets. This control and transport system has the ability to reduce the distortion of the spatial profile of laser plasma accelerated beams and to achieve precise control of the proton beams.

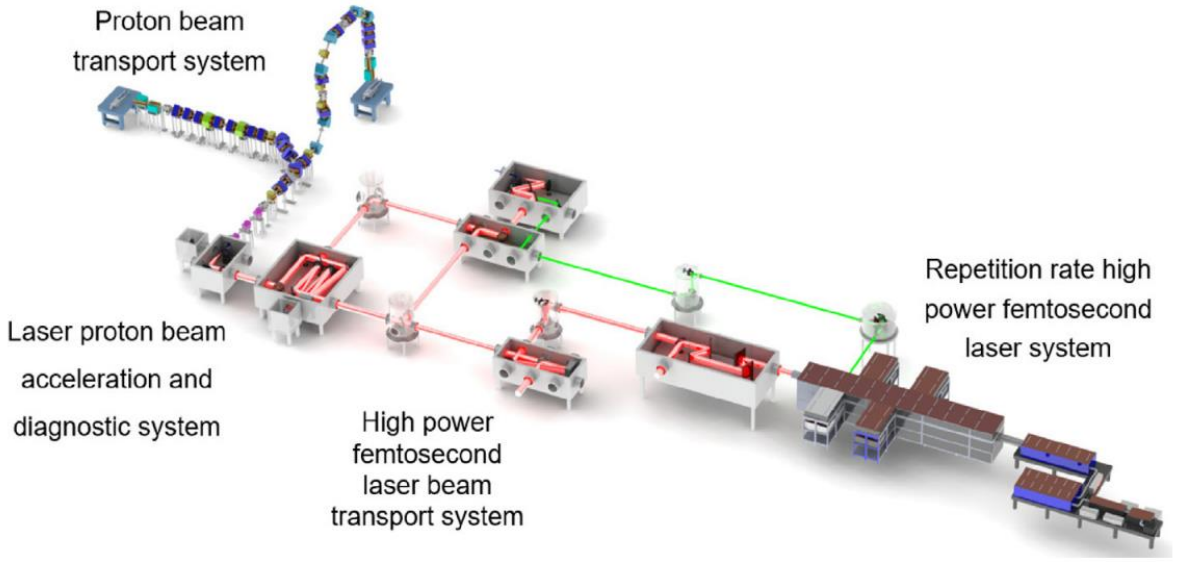

Fig. 2.8. Laser plasma proton accelerator for radiotherapy of malignant tumors built at Peking University with support from the Ministry of Science and Technology of China [264].

Liu Weihao et al [264] showed that due to the dispersion of the accelerated proton pulse, the collimation and change of propagation direction is a problem for the design of laser plasma particle accelerators. Wang et al [264] investigated these issues in the construction of the first laser plasma proton accelerator for the radiotherapy of malignant tumors [265].

CHAPT. 3. CALCULATION ELEMENTS FOR THE DIMENSIONING OF THE HIGH POWER LASER SYSTEM USED FOR PROTON ACCELERATION

In the dimensioning of the laser system, the technique used to obtain the necessary power for the laser beams is based on the amplification of ultrashort chirped pulses. This method received the Nobel Prize in 2018 [146], and assumes that an ultrashort laser pulse is temporally increased, amplified in energy, and compressed to a pulse duration that is given by the ultrashort laser oscillator.

To get a power of 2 PW, the energy after the optical system of temporal shortening (E_{DC}) must be 20 J, and the laser pulse must have a duration (Δt) of 10 fs, according to the equation below:

$$P = \frac{E_{DC}}{\Delta t} = \frac{20}{10 \cdot 10^{-15}\, s} = 2 \cdot 10^{15}\, W \tag{3.1}$$

The optical system for the temporal shortening of laser pulses with four diffraction gratings that recomposes in phase the longitudinal oscillation waves from the electromagnetic structure of the laser pulse has a transmission efficiency of 70%. The rest of the energy is lost by absorption and reflection on the higher scattering orders of the diffraction gratings. As a result, the energy before the optical system of temporal shortening (E_{IC}) will be:

$$E_{IC} = 20 \cdot \frac{100}{70} = 28{,}5\, J \tag{3.2}$$

The intensity depends on the maximum power (P) and the diameter (D) of the laser beam. For a 10 μm diameter Gaussian distribution profile, the laser beam intensity will be:

$$I = \frac{P}{D} = \frac{2 \cdot 10^{15}}{\pi \cdot (0.001/2)^2} = 2.546 \cdot 10^{21}\, W/cm^2 \tag{3.3}$$

The simplified scheme of the 2 PW laser system (Fig. 3.1.) is composed of a laser oscillator, a system to change the repetition rate, an optical parametric preamplifier (OPA), an optical system for temporal growth of laser pulses, a high energy amplifier and an optical system of temporal shortening. The laser oscillator will generate ultrashort pulses of 10 fs and 100 nJ energy with wide spectral bandwidth at a repetition rate of 50 kHz. The pulses generated by the oscillator will be temporally increased to 10 ps by a dispersive glass material (SF11) and the repetition rate will be changed to 1 kHz by changing the polarization of the light in the electro-optical nonlinear medium. Thus, the number of pulses and their intensity are reduced and can be sent to the next module in the composition of the high-power laser system.

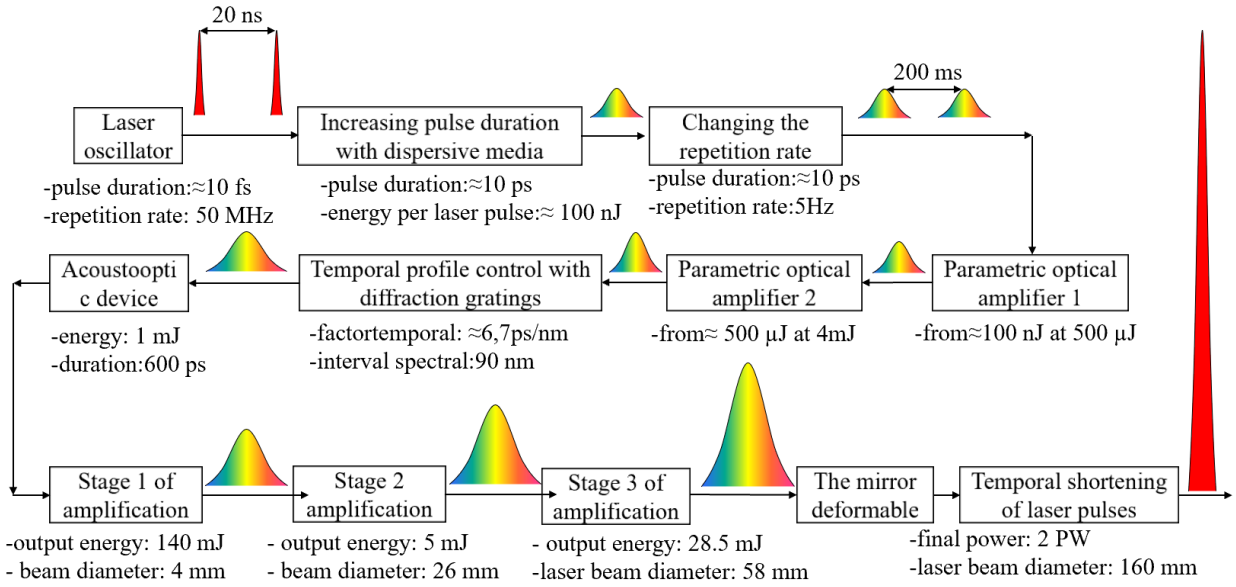

Fig. 3.1. Simplified schematic representation of the 2 PW laser system.

3.1.2. Determination of the pulse duration and repetition rate

The ultrashort pulse oscillator is characterized by a repetition rate that is typically of megahertz order, for an energy level of nanojoules (nJ). Twice the length of the resonator (d) determines the repetition rate (f) and implicitly the distance between two pulses. So, in the case of a resonator with a length of 3 m, during a round-trip beam propagation, the distance will be d = 6 m, from which will result:

$$v = \frac{d}{t}, \quad t = \frac{d}{c} = \frac{2(0{,}7 \cdot 2 + 0{,}65 \cdot 2 + 0{,}3)}{299\,792\,458} = 2 \times 10^{-8} s \tag{3.4}$$

$$f = \frac{1}{T}, f = \frac{1}{2 \cdot 10^{-8} s} = 50\ MHz \tag{3.5}$$

At the repetition frequency of $50\ MHz$, the distance between two adjacent pulses is $20\ ns$. If mirrors with reflective deposits in the range of 700 – 900 nm are used in the resonator, then we will have a central wavelength at $\lambda_0 = 800\ nm$ and we can consider a variable range of wavelengths at pulse width at half height (FWHM) of $\Delta\lambda = 90\ nm$. The relationship between the spectral band and wavelength is as follows:

$$\Delta\nu = \frac{c}{\lambda_0^2}\Delta\lambda = \frac{3 \times 10^8}{(800 \times 10^{-9})^2} 90 \times 10^{-9} = 4{,}218 \times 10^{13}\ s^{-1} \tag{3.6}$$

For a Gaussian spectral profile ΔP, using the Fourier transform at limit, the product of the pulse duration at FWHM and the frequency bandwidth is:

$$\Delta P = 2 \log 2 / \pi = 0{,}4423 \tag{3.7}$$

The pulse duration ΔΓ is inversely proportional to the spectral band of the active medium. The better the optical cavity of the oscillator is aligned, the larger the spectral bandwidth is obtained and consequently the pulse duration becomes ultrashort:

$$\Delta\Gamma = \frac{0{,}4423}{4{,}218 \times 10^{13}} = 10{,}48\ fs \tag{3.8}$$

3.2. Determination of the temporal characteristics of the laser pulse

The energy amplification of ultrashort pulses is only possible by temporally increasing the laser pulse and adjusting the beam size so that the photon density on the surface is below the threshold of destruction for the optical components. Since the output energy available from the amplifiers is dependent on the duration of the input pulse, increasing its time can reduce the peak power by an order of magnitude.

3.2.1. Determination of dispersion characteristics

We consider that the pulse emitted by the oscillator has a Gaussian intensity profile, FWHM of 90 nm and duration at the limit of the Fourier transform [177] of $\Delta t_{FTL} = 10{,}48 \cdot 10^{-15} s$. Time stretching is done by propagating the beam through a glass made of SF11 [270] with a length of 150 mm, at which the group velocity dispersion (GVD) is determined [271]. The general dispersion formula for the refractive index of SF11 glass is given by the Sellmeier equation:

$$n(0.8) = \sqrt{1 + \frac{1{,}73759695 \cdot 0{,}8^2}{0{,}8^2 - 0{,}013188707} + \frac{0{,}313747346 \cdot 0{,}8^2}{0{,}8^2 - 0{,}0623068142} + \frac{1.89878101 \cdot 0{,}8^2}{0{,}8^2 - 155{,}23629}} = 1{,}764 \tag{3.9}$$

The group velocity dispersion for the wavelength of $\lambda = 0{,}8\ \mu m$ was determined to be: $GVD = 187{,}50\ fs^2/mm$. After two passes through the SF11 dispersive material, the group delay dispersion (GDD) expressed as the product of $GVD \cdot L$ will be:

$$GDD = 187{,}50 \cdot 150 \cdot 2\ (passes) = 56\ 250\ fs^2 \tag{3.10}$$

Therefore, the temporal profile of the laser pulse after propagating 2 times through the SF11 material with length L, can be expressed with the following equation:

$$\Delta t_{out} = \frac{\sqrt{{\Delta t_{FTL}}^4 + 16(\ln 2)^2\ GDD^2}}{\Delta t_{FTL}} \tag{3.11}$$

For $\Delta t_{FTL} = 10{,}48\ fs$, and a $GDD = 56\ 250\ fs^2$, the equation (3.11) becomes:

$$\Delta t_{out} = \frac{\sqrt{\left(10{,}48\ \cdot 10^{-15}\right)^4 + 16(ln2)^2 \left(56250\ \cdot 10^{-15^2}\right)^2}}{10{,}48\ \cdot 10^{-15}} = 9{,}56 \cdot 10^{-12} \approx 10\ ps \tag{3.12}$$

3.2.2. Determination of the temporal growth factor of laser pulses

The laser pulse with a duration of approximately 10 ps and a wide spectral band of 90 nm is sent to the "Offner" type temporal growth system [272-274]. The output energy from the OPA module is limited so the diffraction grating will not be destroyed. The diameter of the laser beam at the entrance to the time-advance optical system is expressed as a function of the limiting fluence (F_{limit}) and energy, as follows:

$$F_{limit} = \frac{E_{OPA}}{\pi\left(D_{800}/2\right)^2} \Rightarrow D_{800} = 2 \cdot \sqrt{\frac{4}{\pi\ 150}} = 0{,}1842\ cm \qquad (3.13)$$

The delay time between the marginal wavelengths introduced by the time-advancing optical system will be the total optical path difference relative to the speed of light. The optical temporal (t_{lt}) growth system will have a factor $\zeta_{temporal}$ of:

$$t_{lt} = \frac{dif}{c} = \frac{183{,}16\ \cdot 10^{-3}}{299792458} \cong 610\ ps \qquad (3.14)$$

$$\zeta_{temporal} = t_{lt}/\Delta\lambda\ = \frac{610\ ps}{90\ nm} \cong 6{,}78\ ps/nm \qquad (3.15)$$

3.3. Energy amplifiers for ultrashort laser pulses

3.3.1. Dimensioning of laser beams from parametric optical amplifier

Since the laser pulse entering the OPA must be increased to an energy of 4 mJ from an energy of 100 nJ, the OPA will be divided into two amplification stages. In the first parametric optical amplifier (OPA_1) the energy of the laser pulse is amplified from hundreds of nJ to hundreds of μJ. In the second optical parametric amplifier (OPA_2) the energy of the laser pulse is amplified from hundreds of μJ to several mJ. When propagating through the optical time gain system and the acousto-optic (AO) module, part of the laser pulse energy is diminished by absorption and reflection. The temporal magnification optical system has about 70% [283] energy efficiency, and AO around 40-50%. To obtain an energy of 1mJ at the entrance to the first amplifier, the laser pulse is amplified up to 4mJ of energy.

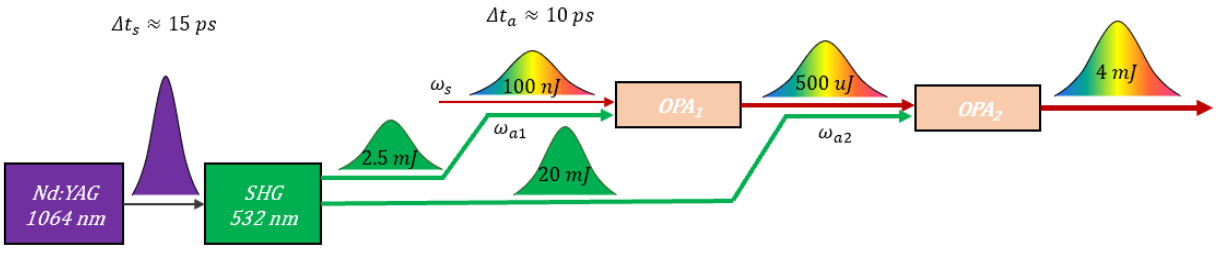

Fig. 3.2. Schematic representation of the power amplifier with two amplification stages OPA_1 and OPA_2. ω_s - main laser beam, ω_{a1}, ω_{a2} - laser beam for amplification [151].

3.3.4. Dimensioning of the two-pass amplifier through the Ti:Sapphire laser medium

The available fluence in the active laser medium (F_{dis}) used in the amplification process will be:

$$F_{dis} = 0{,}9 \cdot 0{,}665 \cdot 0{,}95 \cdot 2{,}433 \; = \; 1{,}383\, J/cm^2 \tag{3.16}$$

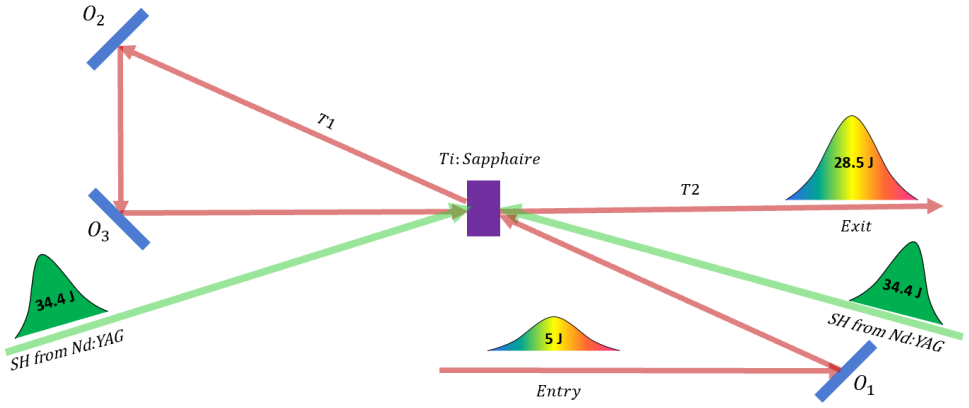

Fig. 3.2. Schematic diagram of the Ti:Sapphire two-pass power amplifier. O_1, O_2, O_3 - plane mirrors, - T_1, T_2 the number of passes of the laser beam through the active medium, SH- second harmonic, Nd:YAG-laser with yttrium aluminum garnet active medium doped with neodymium ions.

After the first pass through the active laser medium, F_{t1} changes according to the equation below, where:

$$F_{t1} = F_{sat}\left\{\ln\left[1+\left(e^{\frac{F_a}{F_{sat}}}-1\right)e^{\frac{F_{dis}}{F_{sat}}}\right]\right\} = 0{,}9\left\{\ln\left[1+\left(e^{\frac{0{,}189}{0{,}9}}-1\right)e^{\frac{1{,}383}{0{,}9}}\right]\right\} = 0{,}662\, J/cm^2 \tag{3.17}$$

Fluency available F_{dis2} in the laser active medium for the second pass (F_{t2}) will be:

$$F_{dis2} = \; F_{dis} - F_{t1} = \; 1{,}383 - 0{,}662 = 0{,}721\, J/cm^2 \tag{3.18}$$

$$F_{t2} = F_{sat}\left\{\ln\left[1+\left(e^{\frac{F_{t1}}{F_{sat}}}-1\right)e^{\frac{F_{dis2}}{F_{sat}}}\right]\right\} = 0{,}9\left\{\ln\left[1+\left(e^{\frac{0{,}662}{0{,}9}}-1\right)e^{\frac{0{,}721}{0{,}9}}\right]\right\} = 1{,}106\, J/cm^2 \tag{3.19}$$

The energy extracted (E_{ext}) from the active Ti:Sapphire laser medium after the 3 passes (E_{t3}) is:

$$E_{t2} = F_{t2} * s = 1{,}106 * \pi * \left(\frac{5{,}8}{2}\right)^2 \cong 29\, J \tag{3.20}$$

$$E_{amp} = E_{t2} - E_{in} = 29 \; - 5 \; = 24\, J \tag{3.21}$$

The calculations were performed considering an uniform intensity distribution for both the laser beam to be amplified, as well as for the population inversion stimulation laser beam. Generally for class 2 PW lasers, Ti:Sapphire active media with dimensions between 80-100 mm diameter and 20-50 mm thickness are required. Laser beams have a diameter between 60-90 mm and a little more in the case of beams used for amplification.

CHAPT. 4. RESEARCH ON THE AUTOMATION OF SOME PROCESSES IN THE COMPONENT OF THE HIGH POWER LASER SYSTEM

4.3. Automation of the optical parametric amplification (OPA) process

In fig. 4.1., both the beam position at λ= 800 nm (ω_s), as well as the beam position at λ = 532 nm (ω_a) will be given by the signal detected by a photodiode. The distance between the two pulses will be compensated by operating the translational mass T_1. Thus, one has a spatial overlap in the direction of the x-axis, of propagation between ω_a with ω_s in the first nonlinear laser active medium BBO_1. The spatial profile adjustment is done with electrically operated mounts MA_1-CCD1 and MA_2-CCD2 for ω_s. Optimizing the energy transfer from ω_s to ω_a is achieved by adjusting the angle for BBO_1 in accordance with the direction of propagation of from the rotating mass R_1. Since the intensity is very high in the center of the beam, part of the photons are converted into amplification energy on the spot.

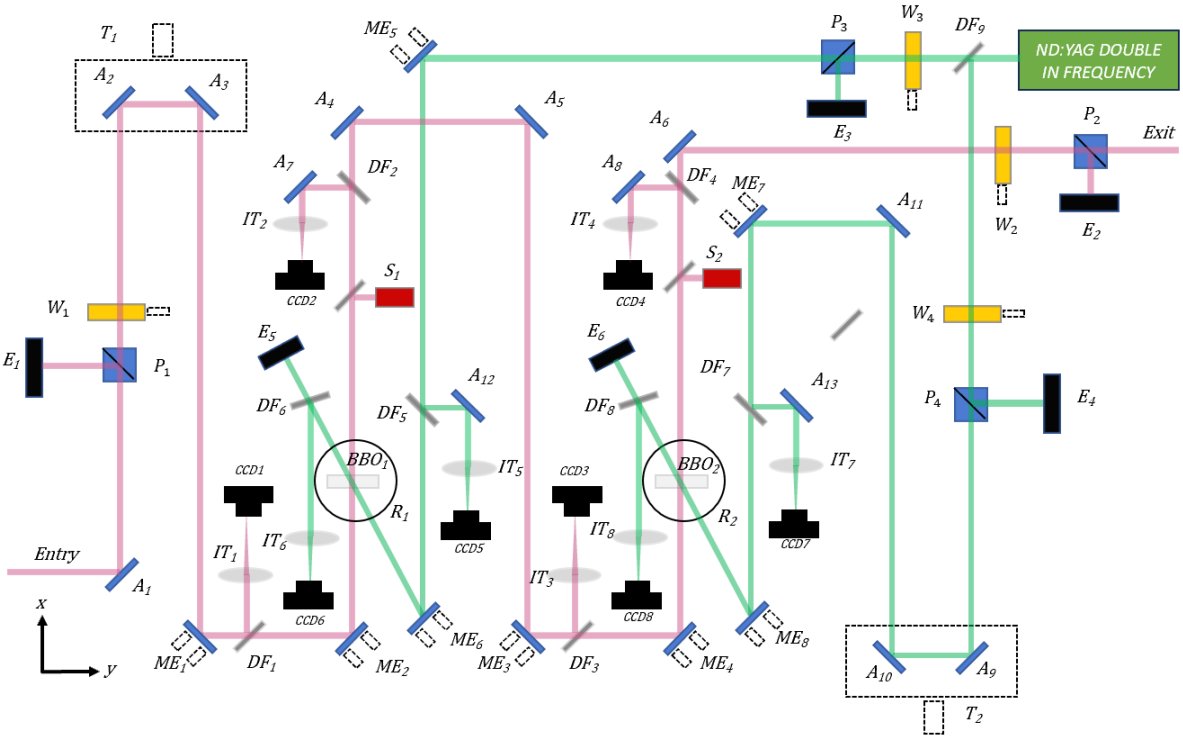

Fig. 4.1. Automation scheme of the parametric optical amplification process with two amplification stages. $L_1, \dots L_{10}$ - lenses for focusing, $CCD_1, \dots CCD_8$- cameras for monitoring laser beams. $DF_1, \dots DF_8$ - beam splitters, $MA_1, \dots MA_8$- electrically operated kinematic mounts, O_1, ...O_{10} - plane mirror, BBO_1, BBO_2 - non-linear laser media, $E_1, \dots E_6$- energy meters, $P_1, \dots P_4$ - cube polarizer. T_1, T_2 - translation stage, S_1, S_2- spectrometers, $W_1, \dots W_4$- optical components with phase change.

The beam that will not be used in the amplification process will be measured with the energy meter E_5 and will represent the response of the α angle control loop. To maintain a wide spectral band of the output pulse, with MA_5-CCD5 and MA_6-CCD6, the position for ω_a will be guided based on the information received from the spectrometer S_1. The method for the amplification process automatic control for OPA_2 is carried out in the same manner, with a small

amendment. Here, the overlap in *BBO₂* on the propagation direction x is carried out by changing the propagation length for ω_s by using the translation stage T_2. A perfect overlap between the two beams is required and this means that the wavelengths combine perfectly.

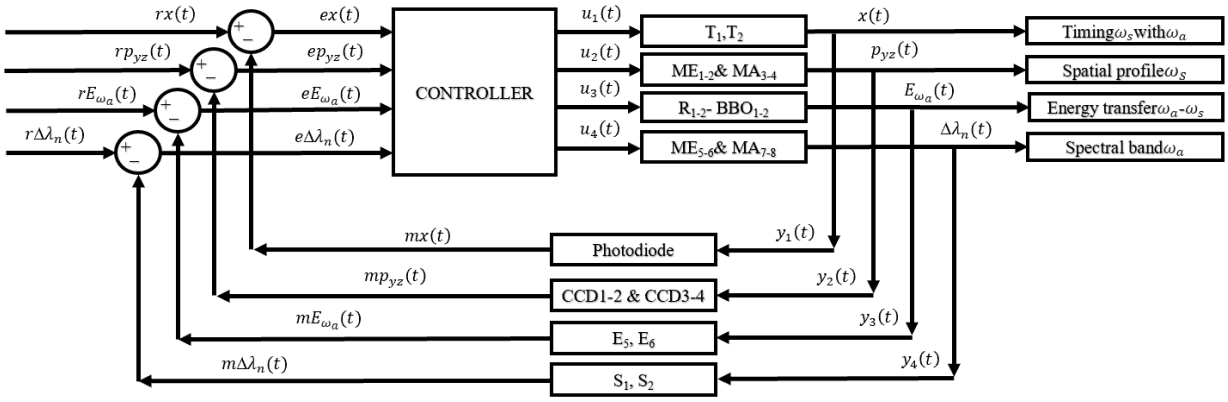

Fig. 4.2. Block diagram for automating the parametric optical amplification process by controlling the synchronization between $\omega_a - \omega_s$, the spatial profile ω_s, the energy transfer from ω_a to ω_s and the spectral band.

The system of equations (4.1) was deduced from the block diagram in fig. 4.2, and this will be implemented in the programming language of the controller to obtain control signals in order to automate the parametric optical amplification process.

$$\begin{cases} ex(t) = rx(t) - mx(t) \\ ep_{yz}(t) = rp_{yz}(t) - mp_{yz}(t) \\ eE_{\omega_a}(t) = rE_{\omega_a}(t) - mE_{\omega_a}(t) \\ e\Delta\lambda_n(t) = r\Delta\lambda_n(t) - m\Delta\lambda_n(t) \end{cases} \qquad \begin{cases} x(t) = y_1(t) \\ p_{yz}(t) = y_2(t) \\ E_{\omega_a}(t) = y_3(t) \\ \Delta\lambda_n(t) = y_4(t) \end{cases} \tag{4.1}$$

The first step to automate the parametric optical amplification process is to spatially synchronize the nonlinear laser active medium. The photodiode will identify the distance between the two laser pulses and provide the current position for ω_a and ω_s with the signal $mx(t)$. If this signal is not equal to the set reference $rx(t)$, a position difference will be obtained $ex(t)$, which must be adjusted. The controller will calculate, according to the first equation, the exact compensation value and will generate the command signal $u_1(t)$, which will actuate the translation tables T_1 and T_2. The propagation length for the two beams must be adjusted until the output signal $x(t)$ will be equal to the reference.

Spatial profile of the beam ω_s can be automatically adjusted from electrically operated kinematic mounts MA_1, MA_2 , at the exit from *BBO₁* and MA_3 and MA_4 on exiting *BBO₂*. The position at which the beam has the desired shape will be given by the signal $p_{yz}(t)$ and will be stored as a reference $rp_{yz}(t)$ relative to the beam position and spatial distribution, parameters observed with the CCD1-4 cameras.

The energy transfer from ω_s to ω_a will be controlled by changing the orientation angle of the active laser medium to satisfy the phase condition between the two signals. The angle adjustment for *BBO₁* is done from the rotation table R1 and for *BBO₂* from the rotation table R_2.

The response of this control loop is given by the signal mE_{ω_a}, measured with energy meters E_5 and E_6. The phase matching angle α will be determined by the lowest value recorded by the energy meters.

Given that the laser pulse has a spectral band ($\Delta\lambda_n \approx 90\,nm$) all wavelengths must be amplified in order not to lose the temporal resolution of the pulse in the optical system of temporal shortening. The spectral band measured with the spectrometer *S1* will be adjusted at the exit from *BBO1* using MA_5, MA_6. This will be done by adjusting the overlap between ω_a and ω_s. The best position at which all wavelengths in the laser pulse are parametrically amplified will be stored as a reference $r\Delta\lambda_n(t)$ and will be given by the information read by the CCD5-6 cameras. In *BBO2* the process of self-adjustment of parametric optical amplification will be done from MA_7, MA_8, according to the spectral band from *S2*.

4.4. Automation of the amplification process in the Ti:Sapphire active media

The output energy and spectral bandwidth of the laser pulse at the end of each amplification stage varies depending on the position at which the two laser beams overlap in the active medium. In other words, the final power of the laser pulse is dependent on both the energy and the spectral band. If some of the wavelengths are not amplified due to an overlap error in the amplification medium, the power of the laser beam decreases. Other problems can also occur, such as amplifying some wavelengths more than necessary, which can ultimately lead to the damage of the high power laser system components.

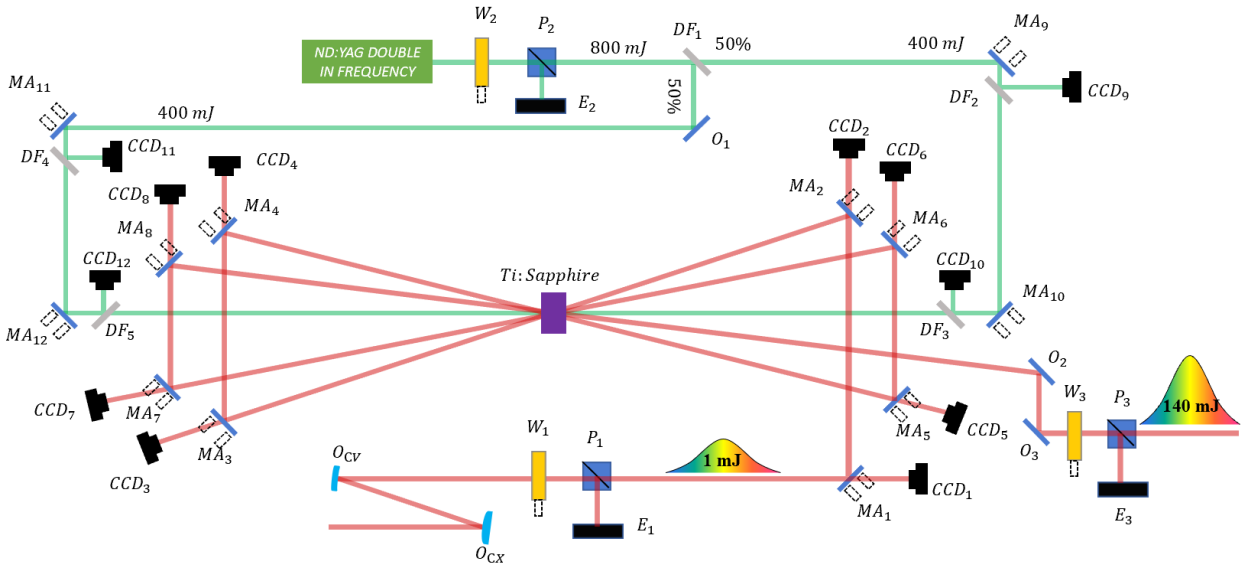

Fig. 4.3. Schematic representation of the optical system for closed-loop monitoring and control of the boost laser beam (green) and the amplified laser beam (red). $CCD_1, \ldots CCD_{10}$ - position detection cameras, $DF_1, \ldots DF_5$, - beam splitters, $MA_1, \ldots MA_8$- electrically operated kinematic mounts, Ocx - convex mirror, Ocv - concave mirror, O_1, O_2, O_3 - plane mirrors, P_1, P_2, P_3- polarizers, E_1, E_2, E_3 - energy meters.

In order to maintain a constant repeatability of the laser beam parameters from one pulse to another, a closed-loop monitoring and control method of the propagation directions for the beams involved in the amplification process was proposed (Fig. 4.3). Laser beam with a central

wavelength of λ= 800 nm(red) is automatically oriented from electrically driven mirrors MA_1 and MA_2, for the first pass through the active Ti:Sapphire laser medium. The position to which it must be oriented is given by the cameras CCD_1 and CCD_2. MA_3 and MA_4, with the related cameras CCD_3 and CCD_4 , are used for an automatic orientation by active laser medium at the second pass. The position of the laser beam for the third pass is monitored by CCD_5 and CCD_6 and is automatically oriented by MA_5 and MA_6. In the last pass the cameras CCD_7 and CCD_8 together with MA_7 and MA_8, are used to have an automatic control and constant monitoring of the position of the laser beam.

The beam generated by the frequency-doubled ND:YAG laser passes through a beam splitter (DF_1) that divides the energy equally. From the mirrors mounted in the electrically actuated kinematic mounts $MA_9, MA_{10}, MA_{11}, MA_{12}$, the two beams used for amplification are automatically oriented. With beam splitters DF_2, DF_3, DF_4, DF_5, a small fraction of the green laser energy is sent to cameras $CCD_9, CCD_{10}, CCD_{11}, CCD_{12}$, in order to monitor the spatial position of the beams for amplification. The block diagram according to which the automatic control system proposed above works is shown in fig. 4.4.

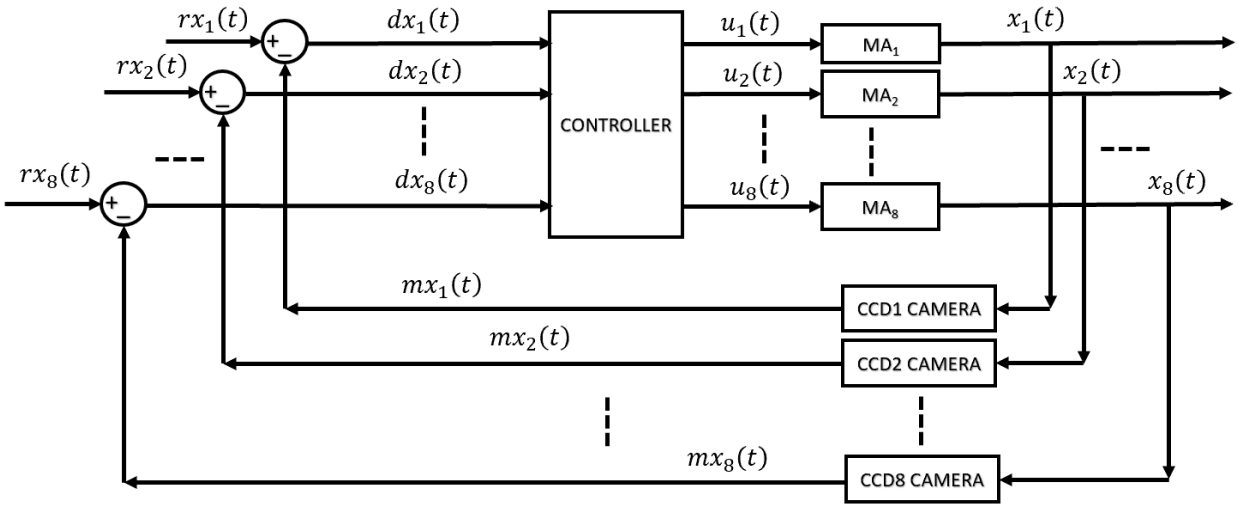

Fig. 4.4. Simplified block diagram for the closed-loop monitoring and control of the laser beam position at each pass through the active laser medium.

If one of the set references $rx_1(t), rx_2(t), \dots, rx_8(t)$is not identical to any of the measured values $mx_1(t), mx_2(t), \dots, mx_8(t)$, then a position difference will be recorded $dx(t)$. Depending on how big the difference between the measured value and the reference value is, the controller will generate the control signals, which will control $u_1(t), u_2(t), \dots, u_8(t)$ electrically operated kinematic mounts, so that the positions of the beams on the surface of the active laser medium $x_1(t), x_2(t), \dots, x_8(t)$ are equal to the references $rx_1(t), rx_2(t), \dots, rx_8(t)$.

$$\begin{cases} dx_1(t) = rx_1(t) - mx_1(t) \\ dx_2(t) = rx_2(t) - mx_2(t) \\ \vdots \\ dx_8(t) = rx_8(t) - mx_8(t) \end{cases} \qquad \begin{cases} x_1(t) = y_1(t) \\ x_2(t) = y_2(t) \\ \vdots \\ x_8(t) = y_8(t) \end{cases} \tag{4.2}$$

CHAPT. 5. DESIGN ELEMENTS OF THE LASER PLASMA PROTON ACCELERATOR FOR THE RADIOTHERAPY OF MALIGNANT TUMORS

The basic structure of the laser plasma proton accelerator for radiotherapy of malignant tumors is based on a high-power laser system, an interaction enclosure for proton acceleration and a system for controlling and directing the proton beams (Fig. 5.1).

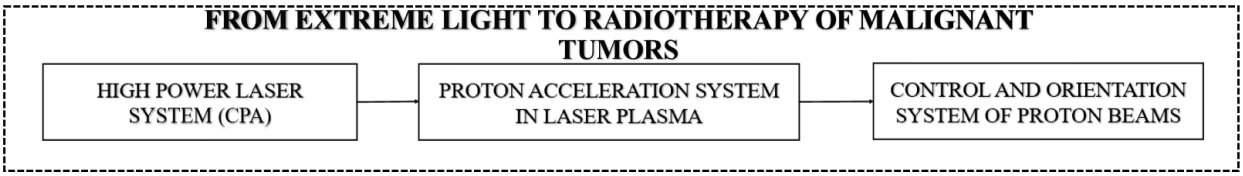

Fig. 5.1. Basic structure of laser plasma proton accelerator for radiotherapy of malignant tumors.

5.7. The high-power laser system used as a proton accelerator

The designed high power laser system is illustrated in fig. 5.2 and is composed of: an oscillator, a pulse selector, a parametric optical amplifier, an optical temporal gain system, three amplification stages, a spatial correction system and an optical temporal shortening system. The oscillator will generate pulses of 10 fs duration, wide spectral bandwidth of 90 nm with central wavelength of $\lambda = 800\ nm$ and 100 nJ of energy which will be directed to the selection system and temporal growth by the dispersion phenomenon. The frequency of 50 MHz is reduced to 5 Hz by changing the polarization using an electro-optical device and the pulse duration is temporally increased from 10 fs to 10 ps in the SF11 dispersive medium. The parametric optical amplifier will use nonlinear BBO laser active media and the laser pulses will be amplified in two stages with an energy of 25 mJ with a wavelength of $\lambda = 532\ nm$. In the first active medium, the laser pulse increases in energy from 100 nJ to 500 μJ, and in the second active medium the laser pulse reaches the energy of 4 mJ. After amplification, the laser pulses are sent to the time-advancing optical system consisting of a diffraction grating and an afocal telescope. Within this optical system, a retroreflector was inserted in a vertical plane so that the laser beam performs a round-trip optical path. At the optical temporal growth system output, the laser pulse has a pulse duration of 600 ps and the energy is reduced to 2.8 mJ, due to the transmission efficiency of 70%. Before the 140 mJ amplifier, the laser pulse passes through an acousto-optical device based on a tellurium oxide (TeO_2) crystal that compensates the higher dispersion orders, generated during the propagation of the laser pulses through the dispersive media of the system. If we assume that the efficiency of the acousto-optic device is 35-40%, the output energy will be about 1 mJ. When passing through the first amplifier, the energy of 1 mJ increases to 140 mJ after four passes through the Ti:Sapphire active medium. Population inversion is achieved using two 0.4 J laser beams coming from the same laser source, but oriented in different directions so that the active laser medium is stimulated on both sides. In the design of this amplifier, the total fluence of the laser beams was limited below 2 J/cm^2. The active laser medium in the first amplifier is 10 mm in diameter and 30 mm in length. At the output of the amplifier, the laser pulse with a diameter of 4 mm is expanded up to 24 mm, in order not to destroy the optical components of the

amplifier 2. The active Ti:Sapphire laser medium with a diameter and a length of 40 mm will use about 15 J of amplification energy, so that the main pulse reaches an energy of 5 J.

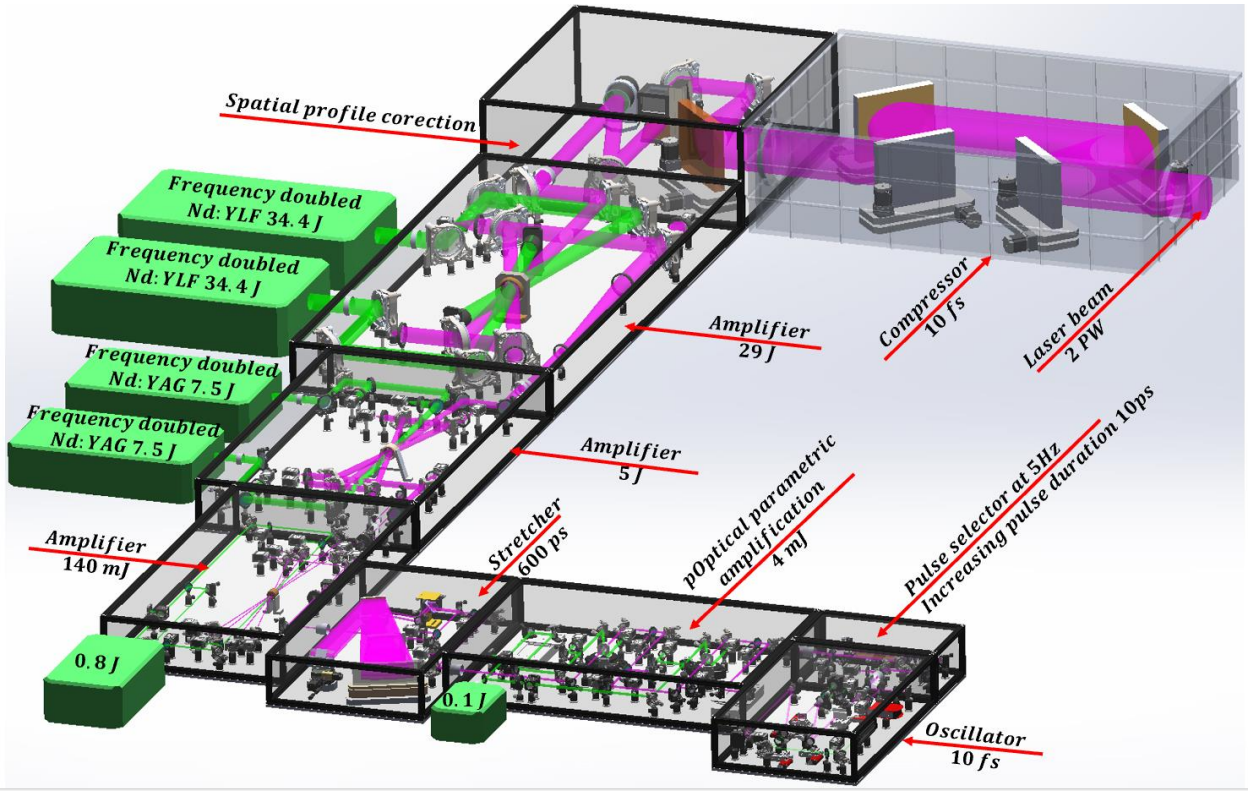

Fig. 5.2. The assembly of the 2 PW laser system used as a particle accelerator.

Table 5.1. Characteristics of the laser beam generated by the high power laser system.

Output energy	Repetition rate	Pulse duration	Spectral range
20 J	5 Hz	10 fs	90 nm

Between the last power amplifier and the temporal shortening optical system, the spatial profile correction optical system with deformable mirror was designed. Since the destruction fluence of the diffraction gratings is limited to 150 mJ/cm^2, upon entering the time shortening optical system, the beam will have a diameter of 160 mm. After diffraction on the first grating, the zero order is sent onto the second grating and the beam becomes collimated but has an optical path difference between the spectral components of the pulse. The distance between RD_2 and RD_3 is chosen so that the spectral components are phase-coupled to shorten the pulse duration to tens of fs. At the exit from the third diffraction grating, the light rays converge and are collimated by the fourth diffraction grating. From the geometry of the time shortening optical system, the oscillation modes are phase-coupled, roughly reproducing the pulse duration generated by the oscillator. Due to the 70% transmission efficiency, the energy is reduced from 28.5 J to 20 J, and the 600 ps duration is reduced to 10 fs, from which a power of 2 PW is achieved.

5.10. The laser plasma proton accelerator for the radiotherapy of malignant tumors

The laser plasma proton accelerator for the radiotherapy of malignant tumors is composed of a high-power laser system, a laser-target interaction chamber, and a proton beam control and transport system (Fig. 5.3). The 2 PW laser system is capable of generating laser pulses with durations of 10 fs and energy of 20 J. These are directed to the proton beam accelerator system by a control and transport system composed of two plane mirrors. In the proton beam acceleration system, the laser beam is focused on the target by a parabolic mirror with a diameter of 10 μm, which enables an intensity of approximately $2.5 \cdot 10^{21}$ W/cm^2. By applying the TNSA mechanism for accelerating protons from solid polystyrene targets $(C_8H_8)_n$, proton beams with pulse durations of 1 ps and energies in the range of 100-200 MeV are obtained.

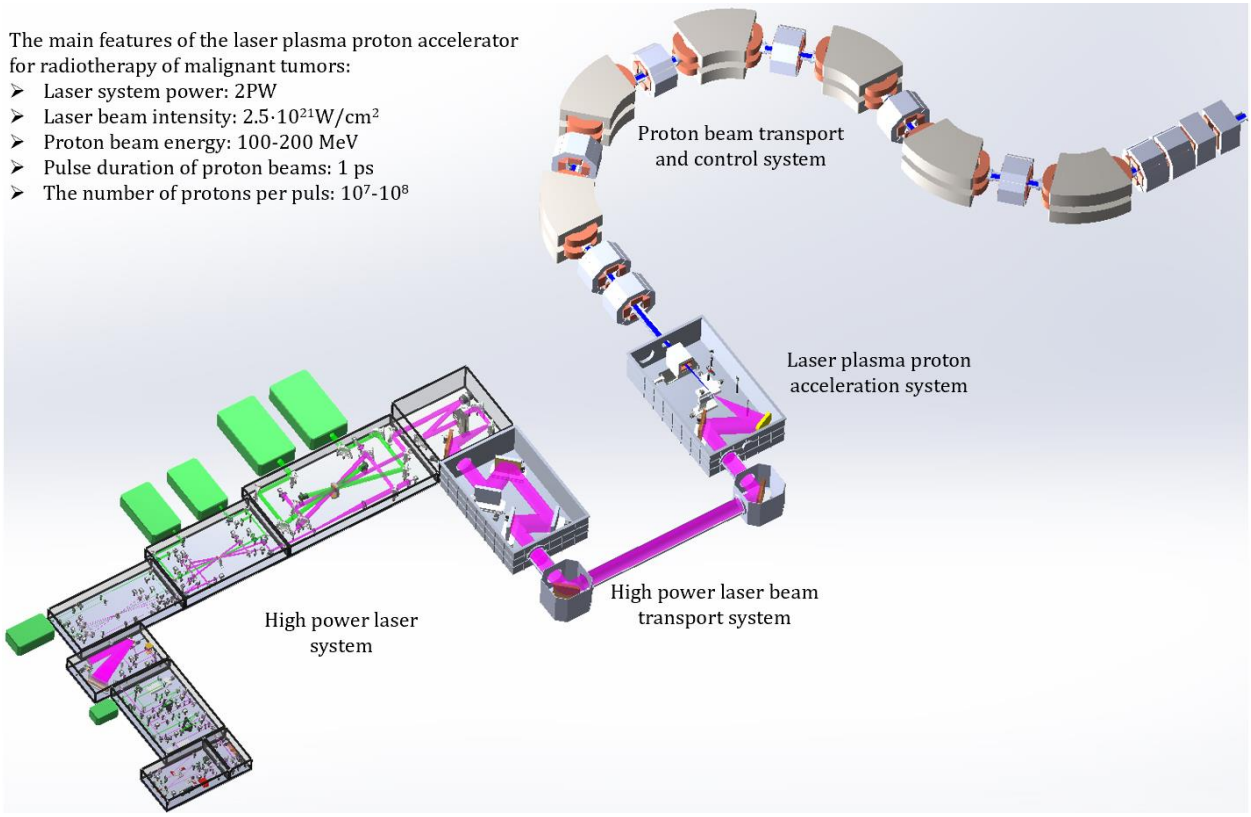

Fig. 5.3. Simplified 3D model of laser plasma proton accelerator for the radiotherapy of malignant tumors.

CHAPT. 6. SIMULATION RESULTS ON LASER-TARGET INTERACTION AND PROTON BEAM DYNAMICS THROUGH THE PROPAGATION DIRECTION CONTROL SYSTEM

6.1. Simplified system for laser plasma acceleration of proton beams

In the proton accelerator system (Fig. 6.1) the laser beam is focused on the target at an angle which prevents backpropagation of laser beam reflections. This phenomenon is due to an intensity contrast with pre and post pulses, high enough to produce the plasma mirror phenomenon that can reflect the main pulse in the opposite direction through the system.

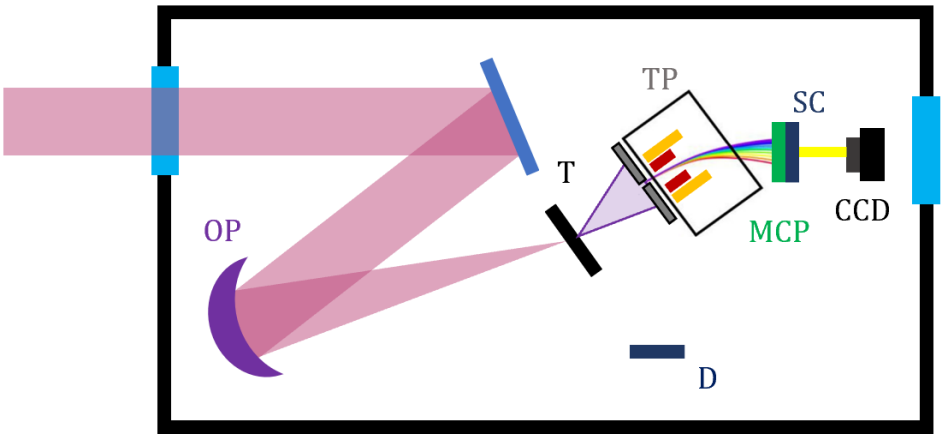

Fig. 6.1. Simplified schematic representation of the proton beam generation system and characterization. OP-parabolic mirror, T-target, TP-proton spectrometer, MCP-particle detector, SC-scintillator, D-detectors, CCD-camera for monitoring laser beams.

In fig.6.1 the laser beam is focused on the target (T) by means of the parabolic mirror (OP) in a diameter of tens of μm. Due to an extremely high intensity, the displacement of electrons from the target will produce a kinetic moment that will accelerate the protons. The emitted proton beam is perpendicular to the target and is sent to the "Thomson Parabola" (TP) spectrometer, which measures the energy spectrum. Behind the TP spectrometer is a micro-channel system (MCP) where protons give up energy to electrons that have a certain electrical charge. By applying a high voltage, this emitted electrical signal is multiplied by the MCP. By measuring the generated electrical current, an estimation of the proton beam energy is being made. A scintillator (SC) is mounted behind the MCP, which will generate a light signal that will be collected by the CCD camera.

For the generation of proton beams, a solid plastic target was proposed, because of the low density, protons can be more easily accelerated to energies of the order of hundreds of MeV [1]. In any case, recent research shows that most experiments studying proton acceleration with high-power lasers report the detection of large numbers of accelerated protons, even when using metal targets [1].

6.1.1. Simulation results on laser-target interaction

For the simulation of the proton emission process [240] we considered a laser beam intensity of 10^{21} W/cm^2, having an energy of 20 J and a pulse duration of 20 fs. The beam was focused into a spot with a diameter of 10 μm at FWHM, on a polystyrene $(C_8H_8)_n$ target with a thickness of 100 nm and a density between 0.96-1.05 g/cm^3.

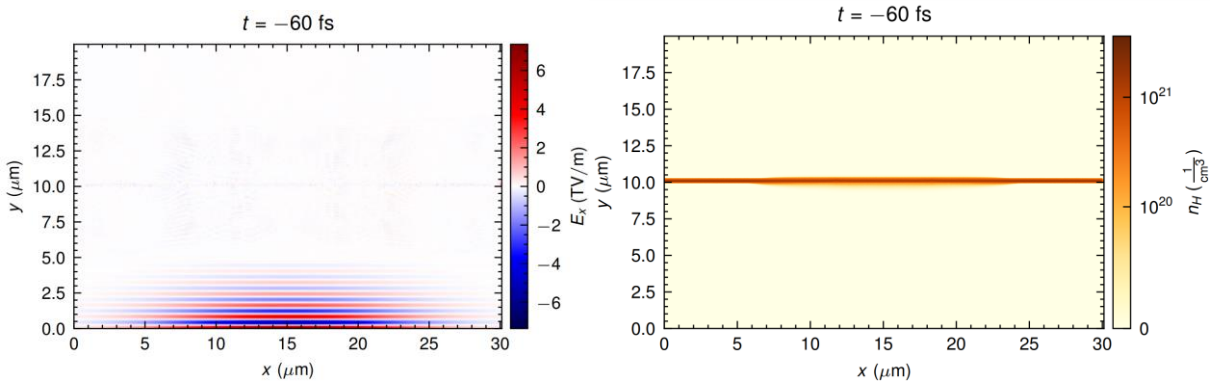

Fig. 6.2. The initial state at the time instant of 60 fs before the interaction of the laser beam with the target. The intensity of the electric field E_x, of the laser beam along the propagation direction y (left) and the dynamic behavior of the protons (n_H) in the target (right).

The laser beam is linearly polarized in the x direction, propagates in the y direction, and generates an electric field intensity of the order of TV/m. The density of the hydrogen layer in the target (the main source of protons) is about $10 \cdot 10^{20}$ cm^{-3}.

When an ultra-intense laser pulse interacts with the 100-nm-thick polystyrene $(C_8H_8)_n$ target, part of the front layer of the target turns into a dense plasma. In this layer, where the laser and plasma frequency are equal, the laser pulse is strongly absorbed, propagating into the region of higher plasma density. The laser beam-plasma interaction obtained at the target surface generates electrons with MeV energies that propagate through the target.

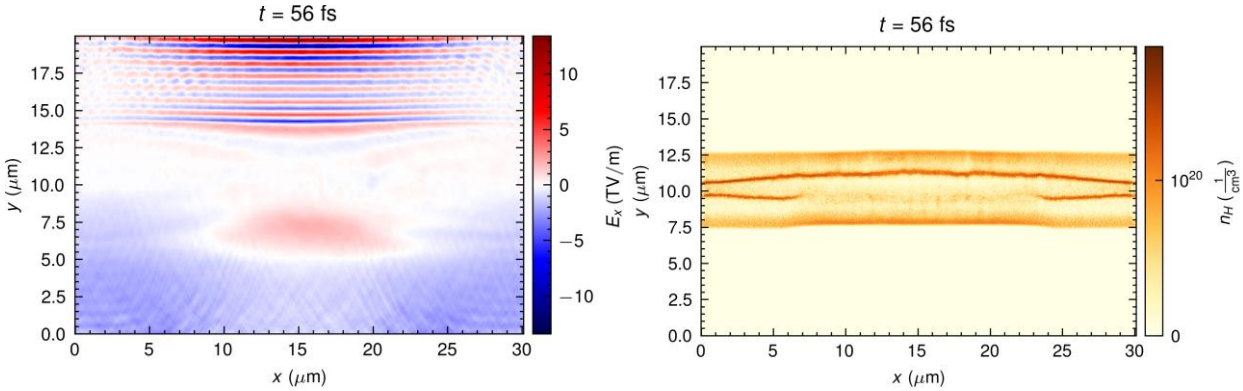

Fig. 6.3. The electric field intensity E_x of the laser beam along the y-travel direction (left) and the dynamic behavior of protons (n_H) in the target at the time instant 56 fs after the laser–target interaction (right).

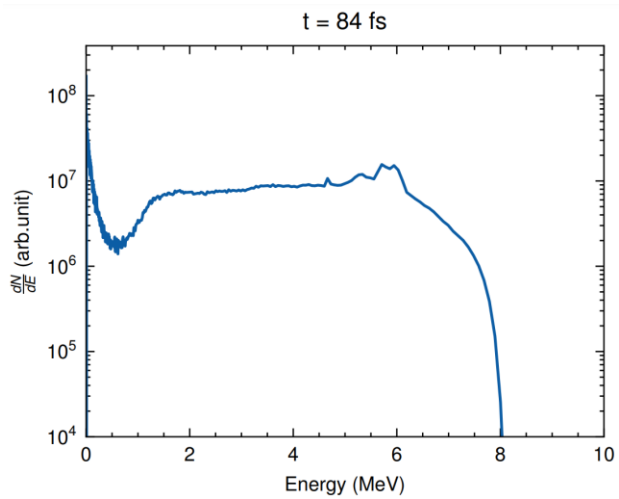

Fig. 6.4. Subatomic proton particle energy spectrum obtained from simulations at the time instant 84 fs after the interaction of the laser beam with the target material.

6.2. Simplified model of the proton beam control and transport system

In the case of the simulations in fig. 6.5, a number of 2000 protons, were defined at the input (red arrow) of the control and transport system. To simplify, we considered that the proton beam is collimated, has a spatial profile with Gaussian distribution and energy of 10^7 eV. The results of the simulations show that only about 350 protons are oriented and controlled until the last element (EMQ_8) of the system. This means that the efficiency of the proton beam control and transport system is below 18%. Ion optics simulations were performed using the *SIMION* simulation environment.

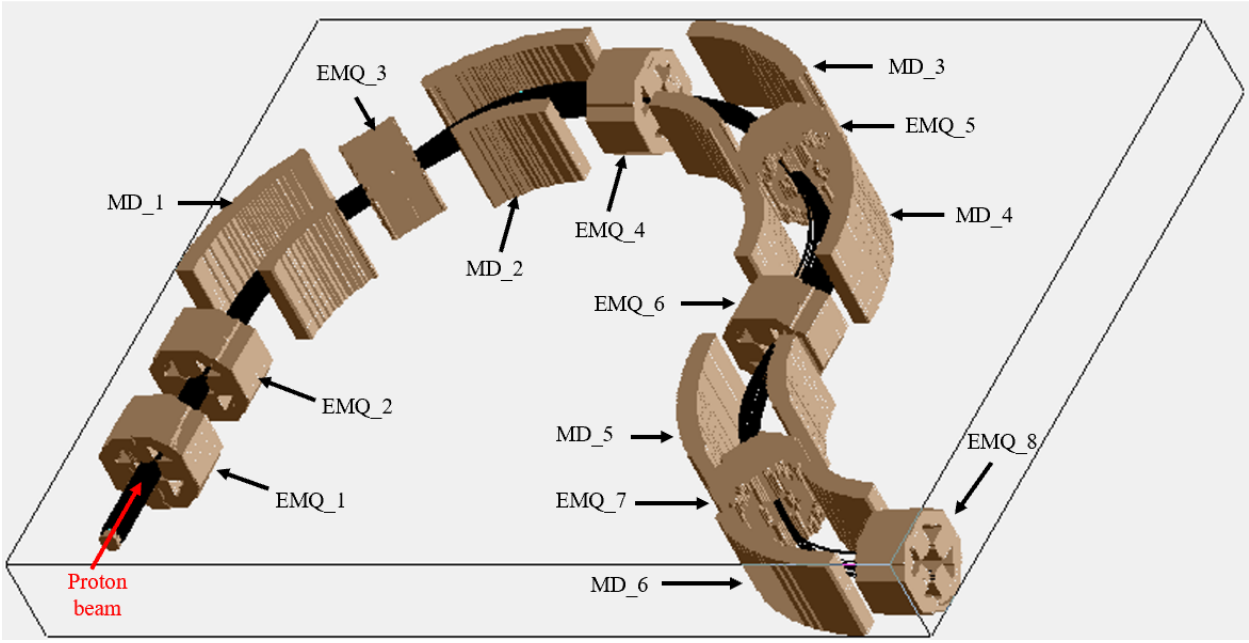

Fig. 6.5. Three-dimensional view of laser plasma accelerated proton beam control and transport system simulations. EMQ_1 ... EMQ_8- 4-pole electromagnets, MD_1 ... MD_6- 45° dipole electromagnet.

CHAPT. 7. RESULTS OF THE EXPERIMENTAL RESEARCH ON THE AUTOMATIC ORIENTATION AND ADJUSTMENT SYSTEMS OF LASER BEAMS

7.1. Results of the experimental research on the testing of the closed-loop laser beam monitoring and guidance systems

7.1.1. Results of research on the automation of the kinematic structures for the automatic orientation of the mirrors

For the electrical actuation of the kinematic mirror orientation structure, two stepper motors were used to orient the mirror on the vertical and horizontal axes. The transmission of the rotational motion from the motor shaft to the screw nut was achieved using gear mechanisms. The automation method is detailed in fig. 7.1.

The driving gear (z_1=10 teeth) was mounted on the stepper motor shaft and the driven gear (z_2 =14 teeth) was fixed on the threaded nut. While the nut performs the rotational motion, the bolt performs the translational motion. The kinematic structure was manufactured by 3D printing and assembled with mechanical elements (Fig.7.1).

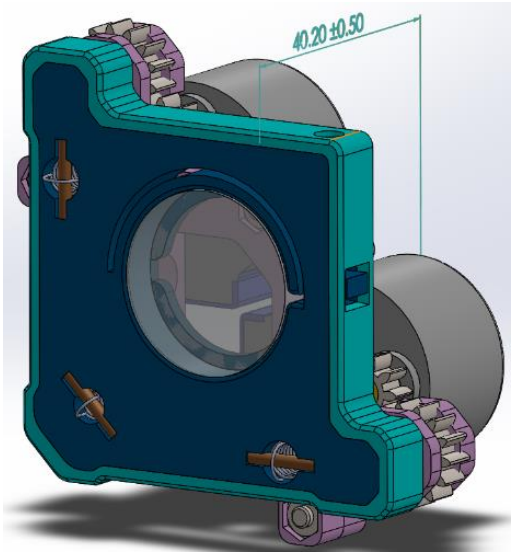

Fig. 7.1. 3D overall model of the kinematic structure with electric drive [191].

The gear mechanism has a rotational motion reduction coefficient (z_1/z_2) of 0.714. The smallest motor shaft rotation corresponds to an angle (γ) of 98.17 mrad. The minimum nut rotation angle (β) will be ($\gamma \cdot z_1/z_2$) 70.097 mrad. At a full rotational movement of the nut (ϕ) (6.283 rad), the bolt performs a translational movement (t) of 4 mm. The theoretical positioning accuracy of the mirror mounted within the kinematic mount is ($\beta \cdot t/\phi$) of 44.95 μm for a motor control signal coinciding with the minimum rotation angle.

7.1.2. Research results on the 3D printing process of the kinematic structures with electrical actuation

Most of the experimental system components were fabricated by extrusion or layer by layer deposition in the desired shape of the material (3D printing). Following the computer-aided design, the designed components were saved with the extension "STL". The structural properties of the 3D printed components were set in the "Cura" software, considering the mechanical stresses to which they are subjected. The 3D printing software has the role of sectioning layer by layer the virtual models and of generating the g-code file to get the physical model. Figures 7.2 and 7.3 detail certain cross-sections of some 3D printed components.

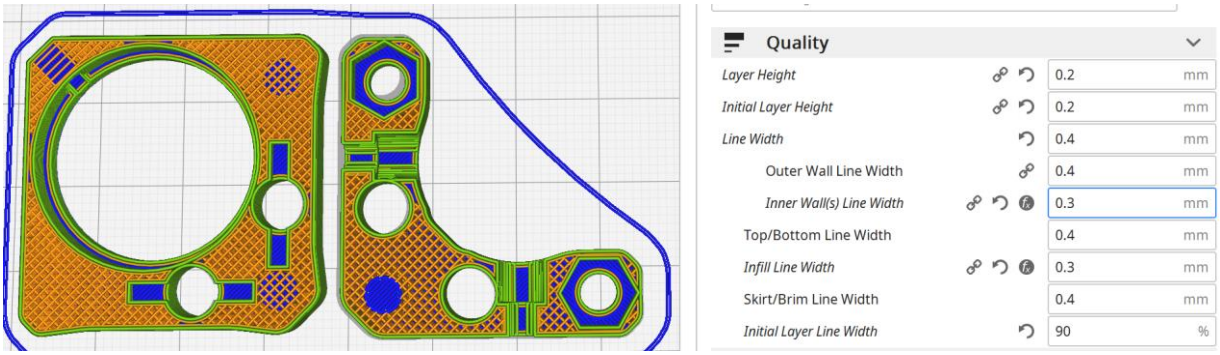

Fig. 7.2. The 3D virtual model of the kinematic clamping structures of the optical beam splitters. On the right side, some of the settings set for the 3D printing process are shown.

In the "Quality" section, the following printing characteristics were set: the height of a layer, in the present case, was 0.2 mm; the width of a single layer deposited to define the edges was set to 0.3 mm and the line width for the material deposited inside, which defines density to 0.3 mm. In the "Shell" section, the following applied settings can be mentioned: the number of lines for printing the outline is 2; the number of solid layers for the bottom and top of the piece is 3.

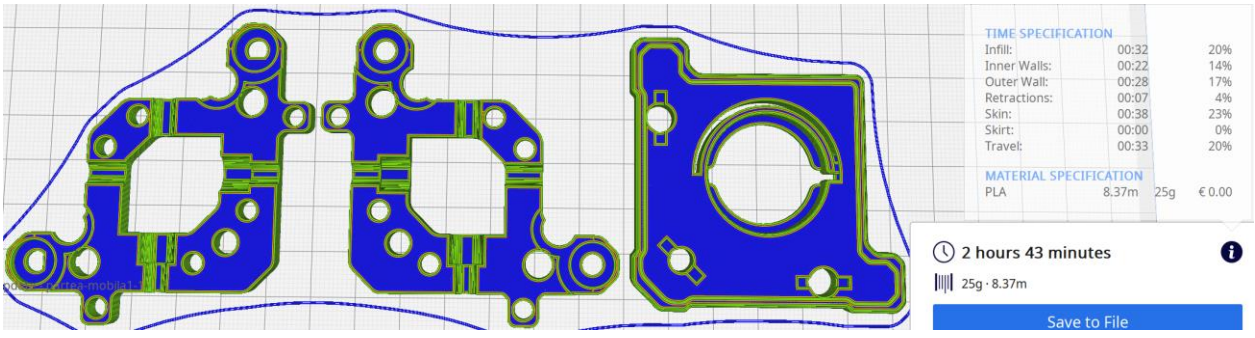

Fig. 7.3. 3D virtual model of the kinematic mount with electric drive. On the right side is displayed the information on the manufacturing time and the amount of used material.

3D printing manufacturing time depends on the material volume of each component and the printing speed. The printing temperature was set to 190ºC.

7.1.3. Research results regarding the modal and structural analysis of the kinematic mirror orientation structures

The mechanical stresses, displacement and vibration modes of the kinematic mount were studied using the COMSOL simulation environment. This is a finite element structural analysis environment. The most important properties of the material used in the simulation were noted in table 7.1. In fig. 7.5 the simulation results regarding the frequencies of the structure's own resonance modes are presented.

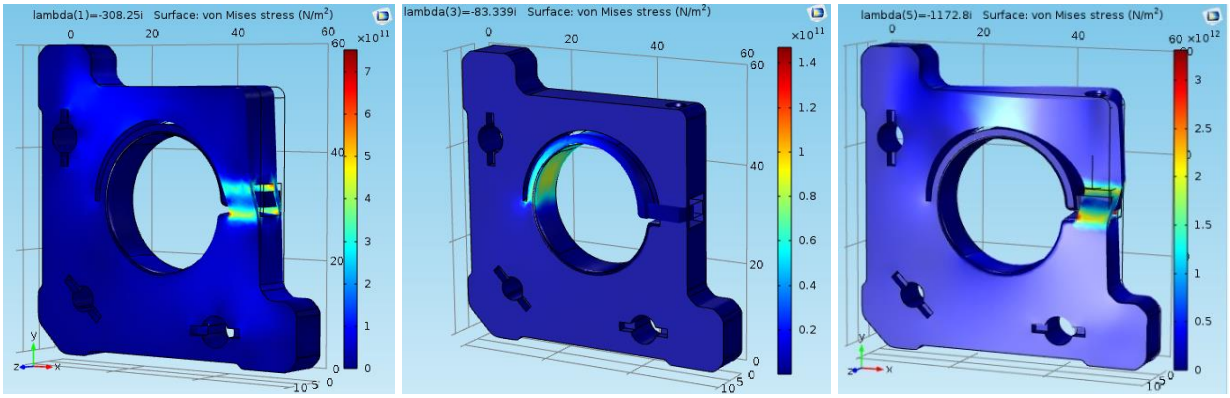

Fig. 7.4. Determination of von Mises stresses by simulating mechanical deformations.

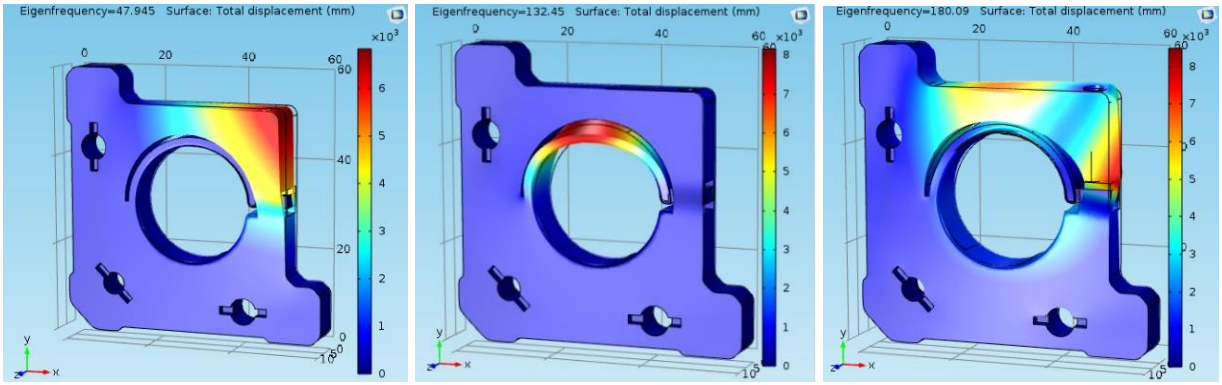

Fig. 7.5. Simulation results on the frequencies of the resonant eigenmodes of the structure.

In fig. 7.4 the most significant mechanical stresses simulated following the application of a force equal to the estimated force of the screw fixing the optical component were presented. Normal stress mode analysis was performed to evaluate the deformation mode. The determination of von Mises stresses is based on the theory of the specific potential energy of shape change. It is widely used in numerical modeling of stress states. It starts from the observation that the materials withstand hydrostatic compression better, which only produces a change in volume, not in shape, compared to the mono-axial one, which clearly changes the shape as well.

7.1.4. Results of the research on laser beam monitoring and the method of automatic mirror orientation

To avoid possible laser beam recognition errors on the CCD camera [291], a digital filter was applied to identify an object according to a certain wavelength that coincides with the wavelength of the laser beam. The algorithm of the applied filter is based on converting the color model obtained by combining colors (RGB) (fig. 7.6. a) into the alternative method of hue saturation value (HSV) representation. In fig. 7.6 c, an example of identifying pink to red objects by applying the RGB-HSV conversion filter is shown (fig. 7.6 b).

Fig. 7.6. Example of identifying and filtering the wavelength detected by the CCD camera. a) original image, b) RGB-HSV conversion and c) final image [191].

7.1.5. Results of the research on the development of the graphic interface for the control of the kinematic mirror orientation structures

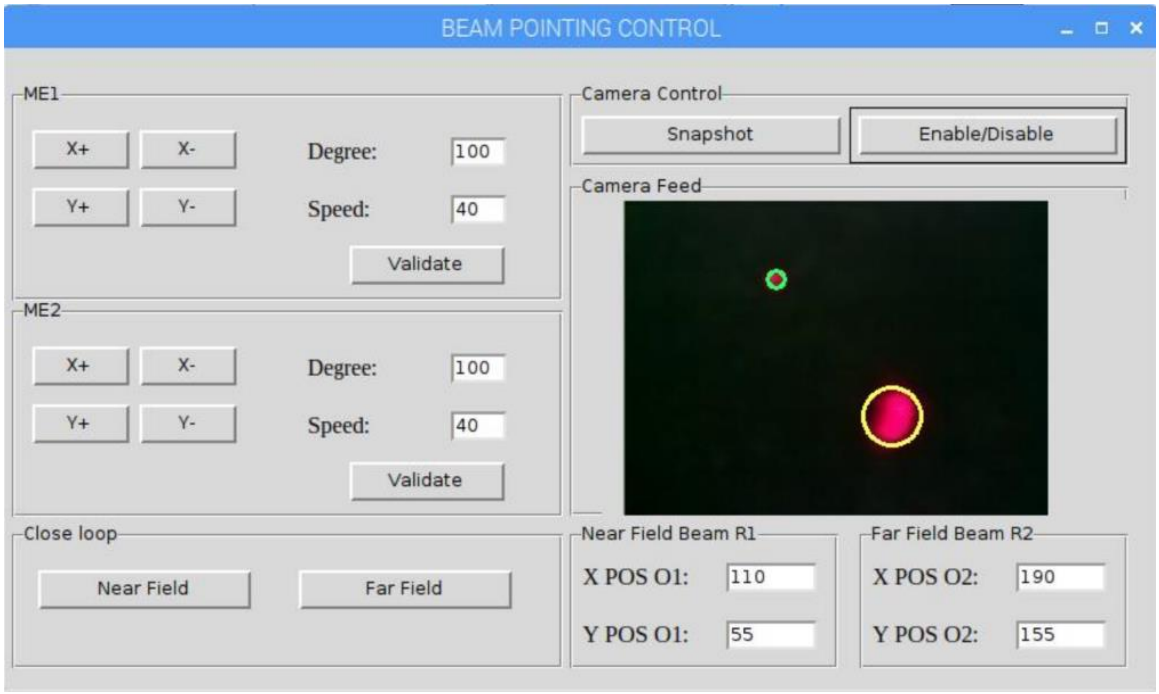

Fig. 7.7. GUI for controlling the laser beam monitoring and tuning system [191].

In the system represented in fig. 7.8., one can see when the beam is not aligned, as it does not pass through the center of the two diaphragms. A displacement on the vertical axis of 35 pixels corresponds to a displacement d_1=3.5 mm on the aperture towards the center of the reference (Fig. 7.7). Also, a displacement of 80 pixels corresponds to a displacement of d_2=8 mm towards the reference, on the first alignment check diaphragm.

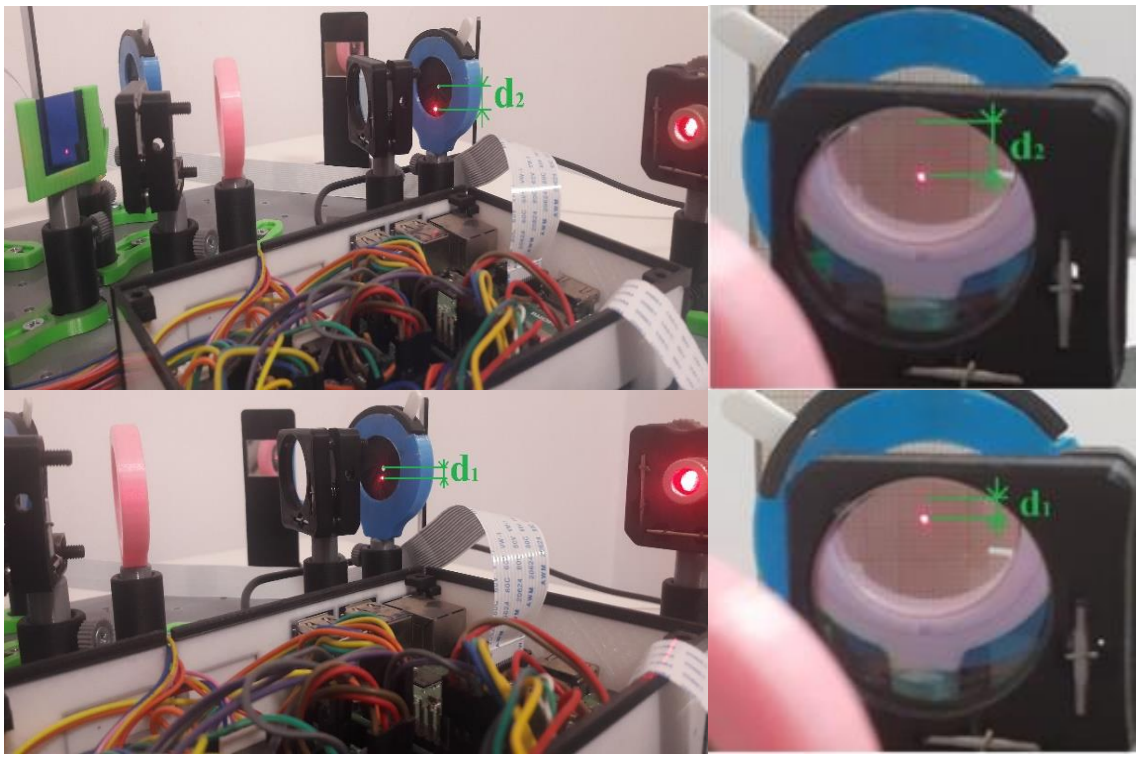

Fig. 7.8. Laser beam positions measured relative to the center of the aperture [191].

In this experimental research, the behavior of a laser beam monitoring and control system was tested. The position changes detected by the CCD camera were processed by the controller which generated electrical control pulses for the execution elements that realize the automatic orientation of the laser beam.

7.2. Results of the experimental research on automatic energy control for laser beams used in the process of ultrashort pulse amplification

7.2.1. Results of the research on the closed-loop control method of the laser beam energy

After the frequency of the fundamental beam has been doubled to λ = 532 nm, a small reflection from the main beam is reflected by the beam splitter and sent to the energy meter which is the responsive element of the system. The beam intensity is adjusted using optical reflection attenuation filters. The energy will be evaluated as a function of the pixel intensity of the CCD camera [307], generated by the beam intensity. The closed-loop control circuit requires the stepper motor to perform rotational movements according to the values read by the energy meter. The Raspberry Pi minicomputer [304] will analyze and compare the acquired data with a

reference value that corresponds to an energy that is desired to be constant during the generation of the laser pulses.

7.2.2. Results of the research on the testing of the laser beam energy control system

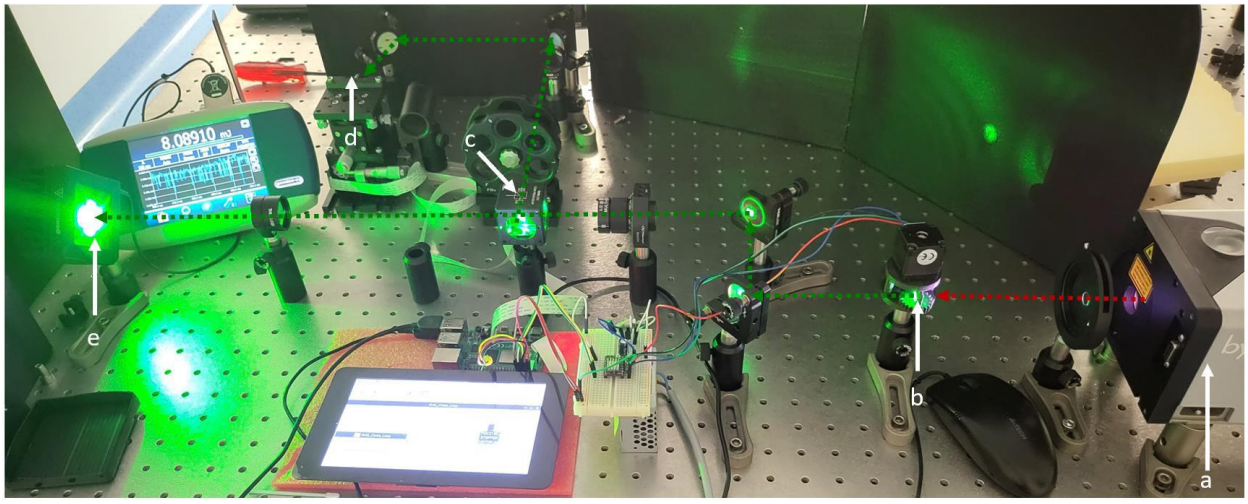

Fig. 7.9. Testing the automatic laser beam energy control system. a- laser with active medium Nd:YAG, b- nonlinear KTP crystal, c- beam splitter, d- CCD camera, e- energy meter [145].

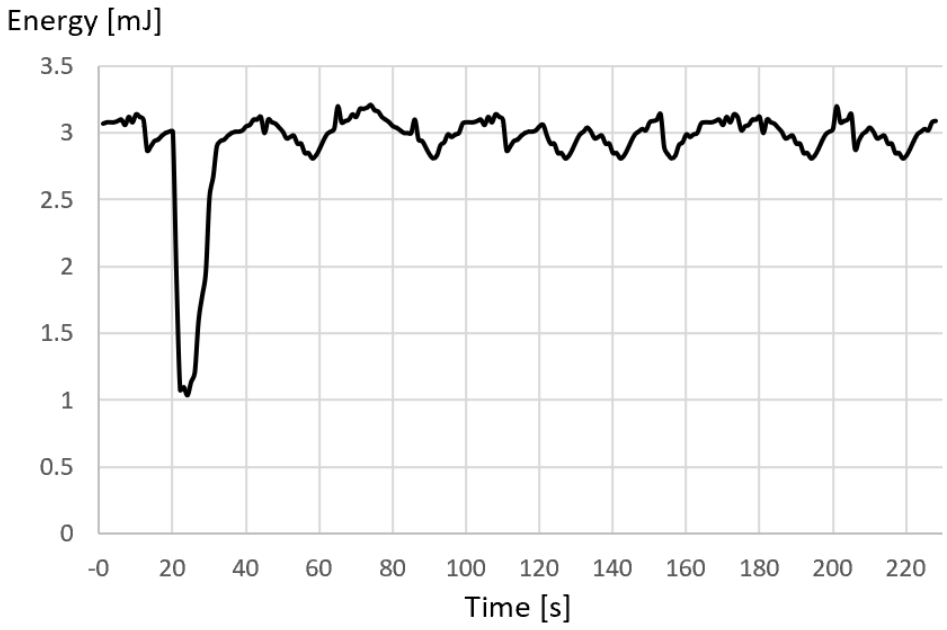

Fig. 7.10. The energy response of the closed-loop control system.

The control system was tested (Fig. 7.9) by changing the supply voltage value of the pumping flash lamps of the Quantel Q-smart 850 laser. In fig. 7.9 a decrease in energy to about 2 mJ is reached when the voltage of the flash lamps is reduced from 650 V to 600 V. The energy meter detects this energy fluctuation and, through the operating conditions of the control

algorithms, the minicomputer transmits the control signals for the readjustment of the second harmonic emission [330]. From this point, the energy gradually increases to the reference value. Also, the energy starts to increase from 1 mJ to 3 mJ. The energy variation around the reference value was in the order of hundreds of μJ according to the measurements represented in fig. 7.10.

7.3. Results of the experimental research on measuring the spatial stability of laser beams

In this research we designed and built a laser beam monitoring system to assess the spatial stability of laser beams from the High Power Laser System at the Extreme Light Infrastructure - Nuclear Physics (ELI-NP) facility [106]. The optical system is based on optical filters for reducing the intensity of the laser beam and a lens for focusing. The spatial stability of the beam is monitored by a CCD camera [307] which has been mounted on a three-orthogonal positioning system. The camera will acquire images by activating the active sensor with external signals generated by the device that synchronizes the high-power laser system at ELI-NP [57, 106, 109]. The processing of the information acquisition and storage algorithms are supported by the "Raspberry pi" hardware [304].

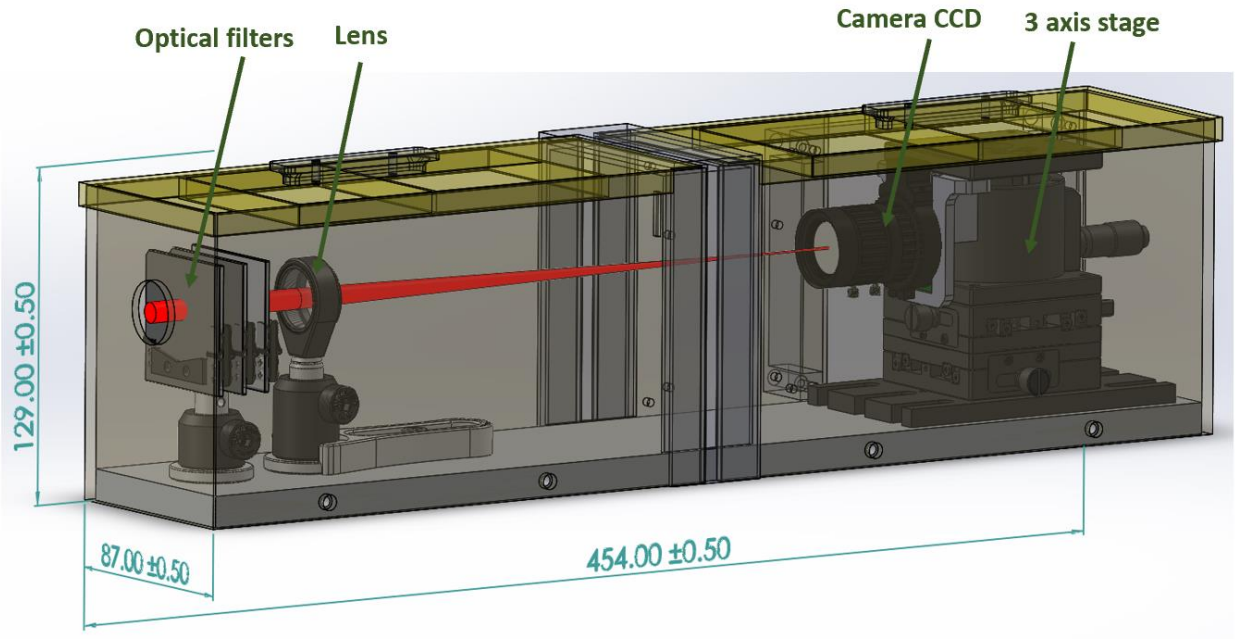

Fig. 7.11. Design of the system for monitoring and measuring the spatial stability of high power laser beams.

Part of the high power laser beam is directed at the entrance into the device (fig. 7.11). Depending on the beam intensity, the attenuation filters are adjusted so that the CCD camera is not saturated. To observe the behavior of the beam in the far field, a lens with a focal length in the range of 250-500 mm is used. The laser beam passing through the lens is focused on the CCD camera.

7.3.1. Results of the research on the testing of the system for measuring the spatial stability of laser beams

The spatial stability measurement system was tested using a laser diode to record data on the positions of the laser beams for certain time intervals. The results regarding the testing of the laser beam stability measurement system are presented in fig. 7.12 and 7.13.

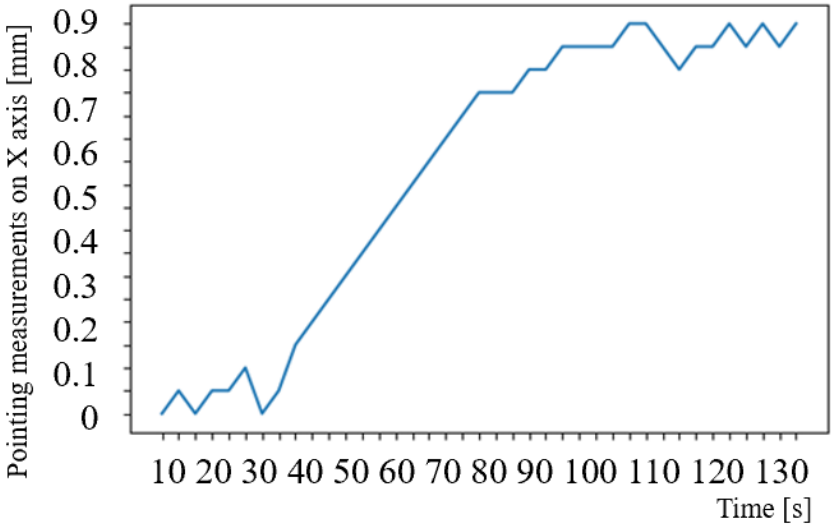

Fig. 7.12. Results of the system testing by measuring the spatial stability of the laser beam on the X-axis.

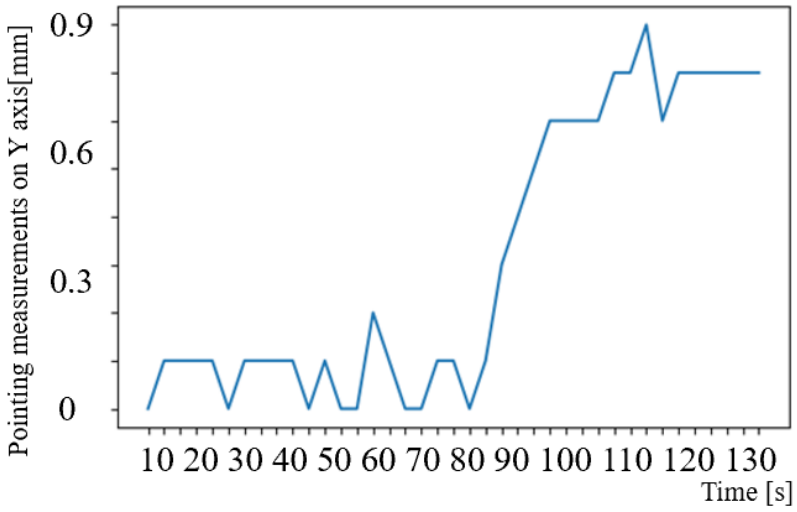

Fig. 7.13. Results of the system testing by measuring the spatial stability of the laser beam on the Y axis.

CONCLUSION

C.1. GENERAL CONCLUSIONS

The main reason why proton beams are desirable in radiotherapy is the inverse dose profile, i.e. a long distance traveled to the biological target with minimal energy loss. The particle's energy is stored until the end of the distance it must travel. Almost all of the energy or Bragg maximum, according to William Bragg, carried by the proton is deposited in the malignant tumor to induce cell death.

Radio frequency accelerators present certain disadvantages such as high implementation costs, the energy of the proton beam depends on the length of the accelerator, the energy spectrum is narrow, the pulse duration is on the order of ns-μs.

Laser plasma particle accelerator technology is under development and has many advantages over the radio frequency particle accelerators. The main advantages that laser plasma particle accelerators present are: small overall size with compact structure, the particles are accelerated over sub-millimeter distances and different species of particles can be accelerated depending on the composition of the material used as a particle source, respectively the time of treatment is reduced due to the ability to irradiate using a high energy spectral range. Compared to radio frequency proton accelerators, laser plasma proton beam exhibit low divergence, large energy spectrum, and nanoampere electrical currents. The pulse duration of few ps and the large spectral range of energy presents the advantage to reduce treatment times by applying higher doses of irradiation. Although these advantages are of interest to the medical field, pulse-to-pulse reproducibility remains an ongoing problem.

C.2. ORIGINAL CONTRIBUTIONS

In the doctoral thesis, I presented the following theoretical, simulation and experimental research:

- testing closed-loop control systems for both automatic laser beam orientation and constant energy maintenance.
- the sizing method of the laser system that can generate an intensity of 10^{20}-10^{21}W/cm^2 (used to accelerate proton beams) as well as its design.
- the integration of automatic control systems in the structure of some subassemblies within the laser plasma proton accelerator.
- the proton beam acceleration method, as well as the laser-target interaction simulation.
- the control and orientation system of proton beams accelerated in laser plasma and the simulation of the dynamic behavior when propagating through the system components.

In the doctoral thesis, the following results were obtained as a result of experimental research, simulation research of some phenomena and the design of some subsystems:

- response times on the order of milliseconds, during experimental research regarding the control and automatic orientation of laser beams that was capitalized by the publication of an ISI-quoted scientific article.
- the graphical interface for the control of 3D-printed and electrically actuated kinematic structures for the automatic orientation of laser beams.

- stability in energy of hundreds of μJ during the testing of the system of automatic adjustment of the energy of the laser beams which was capitalized by the publication of an ISI-quoted scientific article.
- implementation of algorithms for data saving and graphical representation of position changes of laser beams monitored by a CCD camera (research in progress and optimization, which will be capitalized by publication of scientific articles).
- 3D models of the component subsystems within the laser plasma proton accelerator used for the therapy of malignant tumors.
- the dimensions of some optical components within the high-power laser system used to accelerate protons.
- a proton number of 10^7-10^8 and energies of the order of MeV for proton beams accelerated in laser plasma by simulating the laser-target interaction.

C.3. PROSPECTS FOR FUTURE DEVELOPMENT

Due to the growing number of patients with malignant tumors, in the near future the number of radiotherapy centers will increase significantly. The alternative of using laser plasma accelerators for the radiotherapy of malignant tumors is very close to being put into practice due to the advantages it presents.

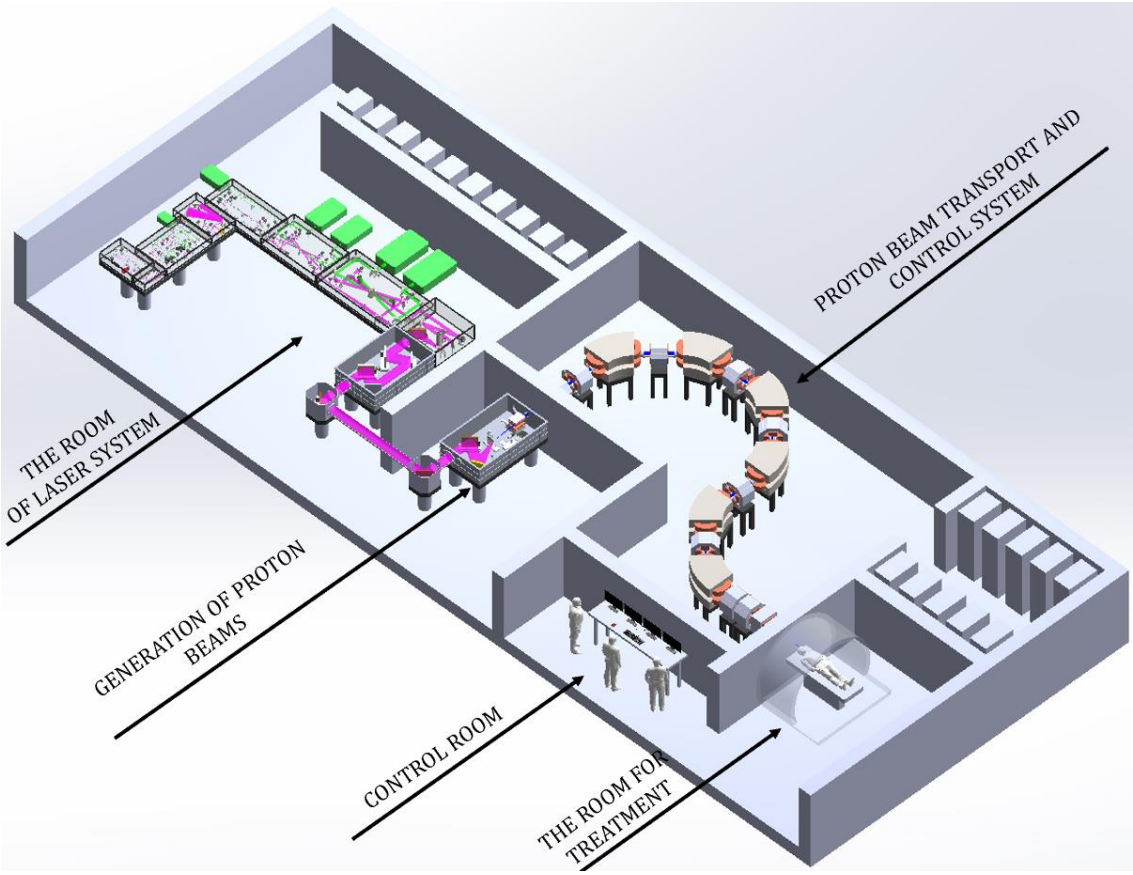

Fig. C.3. Simplified 3D model of a medical center for radiotherapy of malignant tumors with laser plasma accelerated proton beams.

The laser plasma proton accelerator presented in this thesis has realistic dimensions. With certain optimizations, this system could have the chance to be implemented for the radiotherapy of malignant tumors or to serve as a guiding model for the development of these complex systems. By implementing automatic control systems, in a digital system based on artificial intelligence, it would reduce the time and costs related to the operation and control of some operating parameters, as well as the possibility to obtaining reproducible proton beams from one pulse to another.

ANNEXES

APPENDIX 1. LIST OF PUBLISHED WORKS

The research results carried out during the years of doctoral studies were capitalized by the publication of articles in various ISI, BDI or internal indexed journals.

ARTICLES AND SCIENTIFIC PAPERS PUBLISHED AS MAIN AUTHOR:

[1] A. Lazar, O. Dontu, CD Comeaga, "Mechatronic system for monitoring and controlling the direction of propagation of the laser beam" in IEEE 2021 The 12th Int. Symp. Adv. Top. Electrical Eng. March 25-27, 2021, Bucharest, Romania.
[2] A. Lazar, O. Dontu, T. Jitsuno "Automatic control of output energy in frequency-doubled Nd:YAG laser by close-loop the SHG crystal orientation" in Optoelectron. Adv. Mater. Rapid Commun., vol. 17, no. 5-6, 2023, p. 208-213.
[3] * A. Lazar, "Raspberry Pi based IR-Viewer for laser alignment". https://www.eli-np.ro/documents/ELI-NP-Annual_Report-2020-2021.pdf (Accessed on 10.08.2023).

ARTICLES AND SCIENTIFIC PAPERS PUBLISHED WITHIN THE FRAMEWORK OF THE ELI-NP RESEARCH GROUP:

[4] D. Ursescu, D. Matei, M. Talposi, V. Iancu, V. Aleksandrov, G. Bleotu, A. Naziru, O. Tesileanu, M. Rosu, Y. Nakamiya, M. Cernaianu, B. de Boisdeffre, C. Ene, M. Caragea, A. Lazar, M. Kiss, M. Masruri, L. Caratas, A. Toader, D. Nistor, V. Luta, B. Tatulea, D. Popa, N. Stan, T. Jitsuno, R. Banici, A. Baleanu, A. Gradinariu, J. Wheeler, G. Mourou, I. Dancus, "First HPLS Experiments at ELI-NP: Spectral Broadening in Thin Films," in Front. Opt. Laser Sci., edited by B. Lee, C. Mazzali, K. Corwin, R. Jason Jones, OSA Technical Digest (Optica Publishing Group, 2020, pp. LW5G.4.
[5] V. Aleksandrov, G. Bleotu, L. Cartas, R. Dabu, I. Dancus, R. Fabbri, V. Iancu, B. Ispas, M. Kiss, A. Lachapelle, A. Lazar, M. Masruri , D. Matei, M. Merisanu, V. Mohanan, A. Naziru, D. Nistor, R. Secareanu, M. Talposi, A. Toader, A. Toma, D. Ursescu, "Upgrading design of a multi-TW femtosecond laser" in Rom. Rep. Phys., vol. 72, 2020, pp. 413.
[6] I. Dancus, GV Cojocaru, R. Schmelz, D. Matei, L. Vasescu, D. Nistor, A.-M. Talposi, V, Iancu, GP Bleotu, A. Naziru, A. Lazar, A. Dumitru, A. Toma, M. Neagoe, S. Popa, S. Norbaev, C. Alexe, A. Calin, C. Ene, A Toader, N. Stan, M. Caragea, S. Moldoveanu, O. Chalus, C. Derycke, C. Radier, S. Ricaud, V. Leroux, C. Richard, F. Lureau, A. Baleanu, R. Banici , A. Ailincutei, I. Moroianu, A. Gradinariu, C. Caldararu, C. Capiteanu, D. Ursescu, D. Doria, O. Tesileanu, T. Jitsuno, R. Dabu, KA Tanaka, S. Gales, CA Ur , "10 PW Peak Power Laser at the Extreme Light Infrastructure Nuclear Physics–status updates." In EPJ Web Conf., vol. 266, 2022, pp. 13008.

BIBLIOGRAPHY

[1]. Măgureanu A., et al. "Target Characteristics Used in Laser-Plasma Acceleration of Protons Based on the TNSA Mechanism." In Front Phys, vol 10, 2022, pp. 133.
[2]. Wang, WP, et al. "Hollow plasma acceleration driven by a relativistic reflected hollow laser." In Phys Rev Lett, vol 125, no 3, 2020, pp 034801.
[3]. S Khoshbinfar, M Khalili. "Proton beam-driven instabilities in an inclined magnetic field." In Nucl Instrum Meth Phys Res Sect A, vol 1040, 2022, pp 167269.
[4]. Matys, M, et al. "Laser-driven generation of collimated quasi-monoenergetic proton beam using double-layer target with modulated interface." In High Energy Density Phys, vol 36, 2020, pp 100844.
[5]. Junk, T R., L Lyons. "Reproducibility and replication of experimental particle physics results." arXiv preprint, 2020, pp arXiv:2009.06864.
[6]. Lopatin, VS, GE Remnev, MV Zhuravlev. "On Reproducibility of Collective Acceleration of Protons in a Plasma-Anode Diode System." In Russ Phys J, vol 61, 2019, pp 2277-2281.
[7]. Tajima, T, P Chen. "Preface for Special Issue: Progress in Laser Accelerators and Future Prospects." In Photonics, Vol. 10, No. 3, 2023 pp. 292.
[8]. Reimold, M, et al. "Dosimetry for radiobiological in vivo experiments at laser plasma-based proton accelerators." In Phys Medicine Biology, vol 68, vol 18, 2023, pp 185009.
[9]. Wang, KD, et al. "Beam distribution homogenization design for laser-driven proton therapy accelerator." In Nucl Instrum Meth Phys Res Sect A, vol 1040, 2022, pp 167196.
[10]. Bang, W., et al. "Review of laser-plasma physics research and applications in Korea." In J Kor Phys Soc, vol 80, no 8, 2022, pp 698-716.
[11]. Li, Z, Y Leng, R Li. "Further Development of the Short-Pulse Petawatt Laser: Trends, Technologies, and Bottlenecks." In Laser Photon Rev, vol 17, no 1, 2023, pp 2100705.
[12]. Zhao, Y, et al. "Mitigation of laser plasma parametric instabilities with broadband lasers." In Rev Modern Plasma Phys, vol 7, no 1, 2022, pp 1.
[13]. Rosenberg, MJ, et al. "Effect of overlapping laser beams and density scale length in laser-plasma instability experiments on OMEGA EP." in Phys Plasmas, vol 30, no 4, 2023, pp 042710.
[14]. Follett, RK, et al. "Independent-hot-spot approach to multibeam laser-plasma instabilities." In Phys Rev E, vol 105, no 6, 2022, pp L063201.
[15]. Michel, P. "Saturation of Laser–Plasma Instabilities and Other Nonlinear Effects." In Introduction to Laser-Plasma Interactions. Cham: Springer International Publishing, 2023, pp. 371-405.
[16]. Hur, MS, et al. "Laser pulse compression by a density gradient plasma for exawatt to zettawatt lasers." In arXiv preprint, 2022, pp arXiv:2208.08589.
[17]. M Taghavi, H Mosallaei. "Increasing the stability margins using multi-pattern metasails and multi-modal laser beams." In Sci Rep, vol 12, no 1, 2022, pp 20034.
[18]. Aniculaesei, C, et al. "High-charge 10 GeV electron acceleration in a 10 cm nanoparticle-assisted hybrid wakefield accelerator." In arXiv preprint, 2022, pp. arXiv:2207.11492.
[19]. Rehwald, M. "Laser-proton acceleration in the near-critical regime using density tailored cryogenic hydrogen jets.", Technishe Universitat Dresden, Bereich Mathematik und Naturwissenschaften, Fachrichtung Physik, Institut für Strahlenphysik, 2022.
[20]. Wang, KD, et al. "Beam distribution homogenization design for laser-driven proton therapy accelerator." In Nucl Instrum Meth Phys Res Sect A, vol 1040, 2022, pp 167196.
[21]. Reimold, M, et al. "Dosimetry for radiobiological in vivo experiments at laser plasma-based proton accelerators." In Phys Med Biol, vol 68, no 18, 2023, pp 185009.
[22]. Wu, F, et al. "Machine-learning guided optimization of laser pulses for direct-drive implosions." In High Power Laser Sci Eng, vol 10, 2022, pp e12.